

***WT1 transcription factor* impairs cardiomyocyte specification and drives a phenotypic switch from myocardium to epicardium**

Ines J. Marques^{1,2*}, Alexander Ernst^{1,2&}, Prateek Arora^{1,2&}, Andrej Vianin¹, Tanja Hetke¹, Andrés Sanz-Morejón^{1,3,4}, Uta Naumann⁵, Adolfo Odriozola⁶, Xavier Langa¹, Laura Andrés-Delgado^{3,7}, Benoît Zuber⁶, Carlos Torroja³, Marco Osterwalder², Filipa Simões⁸, Christoph Englert^{5,9}, Nadia Mercader^{1,2,3*}

1 Department of Developmental Biology and Regeneration, Institute of Anatomy, University of Bern, Switzerland

2 Department of BioMedical Research (DBMR), University of Bern, Switzerland

3 Centro Nacional de Investigaciones Cardiovasculares CNIC, Madrid, Spain

4 Current address: Molecular Neurobiology, German Cancer Research Center (DKFZ), Heidelberg, Germany

5 Leibniz Institute on Aging-Fritz Lipmann Institute, Jena, Germany

6 Department of Microscopic Anatomy and Structural Biology, Institute of Anatomy, University of Bern, Switzerland

7 Current address: Department of Anatomy, Histology and Neuroscience, School of Medicine, Autónoma University of Madrid, Madrid, Spain

8 Department of Physiology, Anatomy and Genetics, Oxford University, UK

9 Institute of Biochemistry and Biophysics, Friedrich-Schiller-University Jena, Jena, Germany

& These authors contributed equally to this work

*corresponding authors: ines.marques@unibe.ch; nadia.mercader@unibe.ch

Summary statement

Wt1 is a well-studied epicardial marker which is also transiently expressed in a cardiomyocyte precursor pool. Sustained wt1 expression in cardiomyocytes can change their cell fate into epicardial-like cells.

ABSTRACT

During development, the heart grows through addition of progenitor cells to the poles of the primordial heart tube. In the zebrafish, *wilms tumor 1 transcription factor a* (*wt1a*) and *b* (*wt1b*) are expressed in the pericardium, at the venous pole of the heart. From this pericardial layer, the proepicardium emerges. Proepicardial cells are subsequently transferred to the myocardial surface and form the epicardium, covering the myocardium. We found that while *wt1a/b* expression is maintained in proepicardial cells, it is downregulated in those pericardial cells contributing to cardiomyocytes from the developing heart. Sustained *wt1* expression in cardiomyocytes reduced chromatin accessibility of specific genomic loci. Strikingly, a subset of *wt1a/b*-expressing cardiomyocytes changed their cell adhesion properties, delaminated from the myocardium and upregulated epicardial gene expression. Thus, *wt1* acts as a brake for cardiomyocyte differentiation and ectopic *wt1* expression in cardiomyocytes can lead to their transdifferentiation into epicardial like cells.

KEYWORDS

wt1a, *wt1b*, heart development, cardiomyocyte, epicardium, zebrafish, cell fate

INTRODUCTION

The heart is one of the first organs to acquire its function and it starts beating long before cardiac development is completed. In mammals, its function is essential to promote blood flow, to sustain oxygenation and nutrition of the organism. Indeed, heart defects are among the major congenital anomalies responsible for neonatal mortality (van der Linde et al., 2011; WHO, 2020).

The zebrafish is a well-established vertebrate model organism in cardiovascular research given its transparency during early developmental stages, amenable for *in vivo* imaging, and rapid embryonic development (Eisen, 2020). Cardiac precursor cells derive from the anterior lateral plate mesoderm (Stainier et al., 1993). At 14

hours postfertilization (hpf), cardiac precursor cells start to express *myosin light chain 7 (myl7)* (Yelon et al., 1999) and sarcomere assembly begins soon after (Huang et al., 2009; Yang et al., 2014). As the assembly of sarcomeres continues, cardiac precursor cells migrate and fuse into a cone that later forms the heart tube, which is contractile at 24 hpf, and is comprised of a monolayer of cardiomyocytes lined in the interior with an endocardial sheet facing the lumen. Next, the heart tube starts to loop, leading to the formation of the two chambers, the atrium and the ventricle (Stainier et al., 1993). Concomitantly, more progenitors enter the heart tube through the arterial and venous poles (Knight and Yelon, 2016). Around 55 hpf, the outermost cell layer of the heart, the epicardium, starts to form. Epicardial cells arise from the proepicardium, a cell cluster derived from the dorsal pericardium that lies close to the venous pole of the heart. Cells from this cluster are later released into the pericardial cavity and attach to the myocardial surface, forming the epicardium (Peralta et al., 2013; Serluca, 2008).

Wilms tumor 1 (WT1) is one of the main epicardial and proepicardial marker genes and plays a central role in epicardium morphogenesis (Moore et al., 1999; Serluca, 2008). *Wt1* contains 4 DNA binding zinc-finger domains in the C-terminus and has been shown to act as a transcription factor (Hastie, 2017). *Wt1* is transiently expressed in the epicardium during embryonic development and, in the adult heart, is reactivated after cardiac injury (van Wijk et al., 2012; Zhou et al., 2011).

The zebrafish has two *Wt1* orthologues, *wt1a* and *wt1b* (Bollig et al., 2006). These genes are also expressed in the proepicardium and epicardium (Peralta et al., 2013; Serluca and Fishman, 2001) in partially overlapping expression domains. Using transgenic reporter and enhancer trap lines (Bollig et al., 2009; Perner et al., 2007), we previously showed that *wt1a* and *wt1b* are initially expressed in a few proepicardial cells and later in epicardial cells (Andrés-Delgado et al., 2020; Peralta et al., 2014). While *wt1a* and *wt1b* mRNA expression was not detected in the myocardium, *wt1b:eGFP* signal was transiently detected in cardiomyocytes of the atrium close to the inflow tract of the heart. Furthermore, some *wt1a-associated* regulatory regions were found to drive eGFP expression in cardiomyocytes (Peralta et al., 2014). Given that *wt1b* and *wt1a* regulatory elements drive gene expression in the myocardium, but endogenous mRNA expression is observed only in the proepicardium and epicardium, we hypothesized that *wt1* expression in the

myocardium needs to be actively repressed to enable progression of normal heart development.

To explore whether there is a requirement for *Wt1* downregulation in the myocardium for proper embryonic development, we generated transgenic zebrafish models for tissue specific overexpression of *wt1a* or *wt1b* in cardiomyocytes. We found that sustained *wt1a* or *wt1b* overexpression in the myocardium induced the delamination and a phenotypic change from cardiomyocytes to epicardial-like cells. Moreover, we observed impaired cardiac morphogenesis, altered sarcomere assembly, and delayed myocardial differentiation.

ATAC-seq data analysis of cardiomyocytes overexpressing *wt1b* revealed that this regulator acts as a brake for cardiomyocyte differentiation by reducing chromatin accessibility of genomic loci associated with key processes like sarcomere assembly, establishment of apicobasal polarity and adherens junctions formation.

Altogether, our results demonstrate that transcriptional downregulation of *wt1a/b* expression in cardiomyocytes is a prerequisite for cardiomyocyte specification ensuring correct development of the heart and preventing a phenotypic switch of cardiomyocytes into epicardial cells.

RESULTS

Wt1 is downregulated in cardiac progenitors upon their entry into the heart tube

During heart tube growth, cells from the pericardial mesoderm enter the heart tube at the venous pole (Knight and Yelon, 2016). These cells can be labelled with the line *epi:eGFP* (Peralta et al., 2013), an enhancer trap line of *wt1a* (Fig.1A). We found that during this process, cardiomyocyte precursors downregulate eGFP expression concomitant with the activation of *myl7:mRFP* (Fig.1B and Movie 1). We measured the eGFP/mRFP signal intensity ratio in cells of the heart tube, from the sinus venosus (SV) towards the growing heart tube. We found that the further away the cells were from the SV, the lower was the eGFP/mRFP ratio (Fig.1C, n=3).

To further confirm our observations, we performed SMARTer RNA-seq of cells collected from three distinct regions: dorsal pericardium (dp), proepicardium (PE) and heart tube (ht) at 60 hpf (Fig. 1D-F). We detected a gradual decrease in *wt1a* and *wt1b* normalized counts among these three tissues, with the highest counts in PE

cells and lowest in cells from the heart tube. The opposite trend was observed for *myl7* expression, being highest in heart tube and lowest in the proepicardium samples (Fig. 1F).

Next, we performed lineage tracing experiments for *wt1a* to see if a pool of cardiomyocytes was derived from *wt1a* expressing progenitors. We crossed the transgenic fish lines *Tg(wt1a:CreERT2)^{cn10Tg}* with *Tg(-3.5ubi:loxP-EGFP-loxP-mCherry)^{cz1701Tg}* and induced recombination between 1 and 3.5 days postfertilization (dpf). At 5 dpf we analyzed which heart cells expressed GFP, and thus derived from *wt1a* expressing progenitors. As expected, we found that most of the *wt1a*-derived cells were epicardial cells (Fig.1G), but we also found a smaller population of cardiomyocytes that were derived from *wt1a* progenitors (Fig.1G-H'''). In line with these results, previous work (Díaz del Moral et al., 2021) also identified a *Wt1* derived cardiomyocyte pool in mouse hearts. Furthermore, based on single cell transcriptome analysis of embryonic mouse hearts a common early progenitor cardiac pool, for epicardial cells and cardiomyocytes was recently described (Tyser et al., 2021). We decided to study the temporal expression patterns of the epicardial marker genes *Wt1* and *Tcf21* in these progenitor populations (Fig. S1A-A''). We found that *Wt1* but not *Tcf21* is expressed in the epicardial and myocardial common progenitor pool (Me5) at earlier stages. Like our lineage tracing experiments, we observed that at later stages expression of *Wt1* can also be found in a few cells in differentiated cardiomyocytes (Me3), suggesting that they are derived from *Wt1* expressing Me5 progenitor cells. Moreover, during developmental stages, expression of *Wt1* in Me5 decreases, indicating differentiation of the progenitors. These data suggest the existence of a common precursor population both in zebrafish and in mouse.

The observed downregulation of *Wt1* expression during cardiomyocyte differentiation might indicate repression of *wt1* expression in mesodermal precursor cells during myocardial fate acquisition, while high levels are maintained in precursors destined to become epicardium. In line with this possibility there are regulatory elements of the *wt1a* locus that drive expression in the myocardium (Peralta et al., 2014). We wanted to further assess if the observed downregulation of *Wt1* during cardiomyocyte differentiation could be associated with directed repression of *Wt1* gene expression. For this, we inspected previously published data on activating and repressing Histone marks at the *Wt1* genomic locus during four stages of cardiac differentiation from

mouse embryonic stem cells (mESCs) (Wamstad et al., 2012) (Fig. S1B). Low levels of *Wt1* transcripts were visible in mESCs but absent throughout differentiation stages. Similarly, Histone 3 K27 acetylation (H3K27ac) enrichment - which correlates with active promoter and enhancer activity – was present in regions proximal to the *Wt1* transcriptional start site (TSS) in mESCs and mesodermal progenitor cells (Fig S1B). Interestingly, some of these regions also co-localized with enhancer elements known to drive epicardial-specific reporter gene expression (Vieira et al., 2017). Conversely, Histone H3 K27 trimethylation (H3K27me3) signatures, which associate with repressed regions, were near-absent in mESCs, while in cardiac precursor cells and differentiated cardiomyocytes they massively decorated the extended regions flanking the *Wt1* TSS, including the epicardial enhancer elements. Together, these observations indicate that during cardiomyocyte differentiation, *Wt1* expression and epicardial enhancers become actively repressed. In summary, during heart development, cardiac precursor cells downregulate *wt1* upon their entry into the heart tube, which might be a prerequisite for their differentiation into cardiomyocytes (Fig.1I).

Cardiomyocytes that overexpress *wt1* can delaminate from the heart, are depleted of sarcomeric proteins and start expressing epicardial markers

We next aimed at exploring the biological relevance for the observed downregulation of *wt1* in cardiomyocytes. To analyze the consequence of *wt1* expression in cardiomyocytes, we generated the line *Tg(b-actin2:loxP-DsRED-loxP-eGFP-T2A-wt1a)*, to conditionally induce the expression of *wt1a*. Crossing this line into *Tg(myf7:CreERT2)* (Kikuchi et al., 2010) allowed the temporally induced overexpression of *wt1a* in cardiomyocytes. Hereafter, the double transgenic line is called *myf7:CreERT2;eGFP-T2A-wt1a*. We administered 4-hydroxytamoxifen (4-OHT) from 1 to 4 days postfertilization (dpf) to induce recombination of loxP sites and activation of *wt1a* and *eGFP* expression during embryogenesis in cardiomyocytes (Fig. S2A). We confirmed *wt1a* and *eGFP* overexpression in the heart by RT-qPCR (Fig. S2B-E). Comparison of *eGFP* and *wt1a* expression between *myf7:CreERT2;eGFP-T2A-wt1a* with and without 4-OHT administration revealed a 4-fold increase in *eGFP* and *wt1a* expression in the latter (Fig. S2B-E). Moreover, we generated a line to overexpress *wt1b*. We decided to use the Gal4/UAS system in this case, to allow a more homogeneous expression in the myocardium. By crossing

the newly generated *Tg(eGFP:UAS:wt1b)* into *Tg(myI7:Gal4)* (Mickoleit et al., 2014) we specifically overexpressed *wt1b* and *eGFP*, under a bidirectional *UAS* promoter, in cardiomyocytes. The double transgenic line will be hereafter called *myI7:Gal4;eGFP:UAS:wt1b* (Fig. S2F). RT-qPCR data showed that *wt1b* and *eGFP* expression in the heart of the double transgenic line *myI7:Gal4;eGFP:UAS:wt1b* was four-fold upregulated compared to that of the single transgenic *eGFP:UAS:wt1b* (Fig. S2G,H). As a control, we used the double transgenic line *Tg(eGFP:UAS:RFP);(myI7:Gal4)* (Sanz-Morejon et al., 2019), hereafter named *myI7:Gal4;eGFP:UAS:RFP*. RT-qPCR analysis also indicated that expression of *wt1a* and *wt1b* could be monitored via GFP imaging (Fig. S2F-H). Using these new lines, we analyzed the effect of sustained *wt1a* and *wt1b* overexpression in cardiomyocytes during heart development (Fig. 2A). In *wt1a*-overexpressing hearts but not in controls, we observed eGFP-positive cardiomyocytes located apically, protruding towards the pericardial cavity at 5 dpf (Fig. 2B-C'''). Moreover, these delaminating cardiomyocytes showed reduced expression of Myosin Heavy Chain (MHC), suggesting the loss, to some extent, of the myocardial phenotype (Fig. 2C-C'''). We quantified how many of the delaminating cells were GFP⁺ or GFP⁻ and found that only GFP⁺ cells were delaminating, indicating that this delamination process is due to a cell-autonomous effect of *wt1a* in cardiomyocytes (Table S1). We detected a similar occurrence in *wt1b* overexpressing hearts. Here, we also observed GFP-positive and MHC-negative cells that delaminated and adhered to the apical surface of the myocardium, starting at 3 dpf (Fig. 2D-E''').

To better understand the origin of these apically positioned eGFP-positive cells, in the *wt1b* overexpression hearts, we performed *in vivo* imaging in *myI7:Gal4;eGFP:UAS:RFP* and *myI7:Gal4;eGFP:UAS:wt1b* between 2 and 3 dpf (Fig. 2F,G and Movie 2). In *myI7:Gal4;eGFP:UAS:wt1b* hearts, some eGFP-positive cells started to round up and initiated delamination from the myocardium. Cells gradually changed from a flat to a rounded shape and ultimately remained adherent to the outer myocardial layer (Fig. 2G and Movie 2; n=4). This event of cell delamination was not observed in *myI7:Gal4;eGFP:UAS:RFP* control embryos (Fig. 2F and Movie 2; n=2). Apical extrusion of cardiomyocytes can be a consequence of myocardial malformation during which extruded cells are eliminated (Gentile et al.,

2020; Rasouli et al., 2018). However, here we found that the delaminated cells remained attached to the myocardial surface. Between 5 and 6 dpf, these delaminated cells lost their rounded shape and flattened, acquiring an epicardial-like morphology (Fig. 2H-I and Movie 3, n=4).

To confirm that this type of cellular delamination with loss of MHC expression was specific of the overexpression of *wt1* we generated the *Tg(eGFP:UAS:tcf21)* to overexpress another well-known epicardial marker, *tcf21* (Kikuchi et al., 2011), in cardiomyocytes (Fig. S3A,B,B'). We then crossed the *Tg(eGFP:UAS:tcf21)* into the *Tg(myf7:Gal4)* (Mickoleit et al., 2014) to overexpress *tcf21* in cardiomyocytes. Contrary to what we observed when overexpressing *wt1a/b* in cardiomyocytes (Fig. S3C-E"), in the large majority of *myf7:Gal4; eGFP:UAS:tcf21* embryos (59/62) we did not observe apical delamination. In the few cases where delamination occurred (3/62), the protruding cells still expressed MHC (Fig. S3D-D"). Moreover, to assess if the detected changes were specific of the overexpression of *wt1* in cardiomyocytes we overexpressed *wt1b* in other cardiac cells. We crossed *Tg(eGFP:UAS:wt1b)* into *TgBAC(nfatc1:GAL4ff)^{mu286}* (Pestel et al., 2016), to overexpress *wt1b* in the atrioventricular valves (Fig. S3F-F") and *Tg(fli1a:Gal4)^{y1Tg}* (Herwig et al., 2011), to overexpress *wt1b* in the endocardial cells (Fig. S3G-H"). We could not detect any apical delamination, looping defects or reduced MHC expression in these hearts at 3 dpf and 5 dpf.

Due to the position and change of morphology of the delaminated cells we hypothesized that these cells had undergone a change of fate. For a better characterization of a possible switch to an epicardial fate we performed immunofluorescence labeling with the epicardial markers Aldehyde dehydrogenase 2 (Aldh1a2) (Niederreither et al., 2002; Sugimoto et al., 2017) and Caveolin 1 (Cav1) (Grivas et al., 2020) (Fig. 3A and Fig. S4A-I"). We detected GFP/Aldh1a2 double positive cells in *wt1b* overexpression hearts (n=3) but not in controls (n=4) (Fig. 3B-C"). Similarly, whereas in control hearts (n=6) we could not observe GFP/Cav1 double positive cells (Fig. 3D-D"), in *wt1b*-overexpressing hearts (n=4), we identified GFP positive cells that also expressed Caveolin 1 (Fig. 3E-E"). We also detected eGFP⁺ cells within the epicardium of *wt1a* overexpressing hearts, but not in controls (Fig. 3F-I", and Fig. S4B-E"). These eGFP⁺ cells did not express MHC and were Aldh1a2-positive (Fig. 3F-G" and Fig. S4D-E") as well as Caveolin 1 positive (Fig. 3H-I" and Fig. S4F-I"). We also tested for the colocalization of *wt1a*-expression in

cardiomyocytes with a third epicardial marker, *transglutaminase b* (*tgm2b*) (Weinberger et al., 2020). We performed *in situ* hybridization against *tgm2b* mRNA followed by immunohistochemistry against eGFP (Fig. S4J-M'). In non-recombined *myl7:CreERT2; eGFP-T2A-wt1a* hearts, *tgm2b* expression was only visible in few epicardial cells and we could not observe any co-localization with eGFP expressing cells (Fig. S4J-L'). However, in embryonically recombined *myl7:CreERT2; eGFP-T2A-wt1a* hearts, we could observe cells co-expressing *tgm2b* and eGFP located within the epicardium (Fig. S4K-M').

These results suggest that upon sustained ectopic overexpression of *wt1a/b*, cardiomyocytes can delaminate apically from the myocardial layer and adopt features of epicardial cells that contribute to the formation of the epicardium.

***wt1b* overexpression disrupts cell-cell contacts and the basement membrane of the cardiomyocytes**

We decided to get a better understanding on the cellular mechanisms underlying cardiomyocyte apical delamination upon *wt1* overexpression (Fig. 4A). Previous reports showed that correct development and morphogenesis of the heart requires cell-cell adhesion and polarization of the cardiomyocytes (Phillips et al., 2007). The proper localization of tight junctions and adherens junctions has conventionally been used to assess the cell polarity (Zihni et al., 2016). We first performed immunostaining against ZO-1, a component of the tight junctions (Stevenson et al., 1986) (Fig. 4B-E'). Whereas the *myl7:Gal4:eGFP:UAS:RFP* control hearts (n=6) showed discrete apical localization of ZO-1 (Fig. 4B-C'), in *myl7:Gal4:eGFP:UAS:wt1b* hearts (n=8) ZO-1 levels were reduced, the signal was diffuse and not clearly localized to apical junctions between cardiomyocytes (Fig. 4D-E'). This suggests defects in the formation and localization of tight junctions upon *wt1b* overexpression. To evaluate the formation of adherens junctions, we crossed the *Tg(myl7:cdh2-tdTomato)^{bns78}* line (Fukuda et al., 2017) with *myl7:Gal4:eGFP:UAS:wt1b*. This allowed us to specifically visualize subcellular localization of *cdh2-tdTomato* in *wt1b*-overexpressing cardiomyocytes and control siblings (Fig. 4A and F-M'). At 5 dpf, in control embryos (n=6), *tdTomato* signal was clearly localized to cell-cell junctions (Fig. 4f-g) and detected apically in cardiomyocytes (Fig. 4H-I'). In contrast, *myl7:cdh2-tdTomato;myl7:Gal4:eGFP:UAS:wt1b* hearts (n=8), showed a diffused and patchy

staining for *cdh2*-tdTomato, which was not restricted to the apical side of the cardiomyocytes (Fig. 4J-J'' and L-M'). Moreover, we observed loss of *cdh2*-tdTomato signal in the delaminating cells further indicating a loss of polarity in these extruding cells (Fig. 4K-K''). To confirm the impairment in the formation of adherens junctions we did an immunostaining against β -catenin (Fig. 4N-Q'), a core component of adherens junctions (Sheikh et al., 2009). Similar to what we had observed for *cdh2*-tdTomato, β -catenin staining was located at the apical side of cardiomyocytes in *myl7:Gal4:eGFP:UAS:RFP* control hearts (n=5) (Fig. 4N-O'). However, in *wt1b*-overexpressing hearts (n=5) β -catenin staining was no longer detected (Fig. 4P-Q'). Taken together, this data shows that sustained expression of *wt1b* in cardiomyocytes leads to the mislocalization of tight junctions and adherens junctions, indicating an impairment of the apical domain in cardiomyocytes.

To understand the basal domain landscape of cardiomyocytes we performed an immunostaining against Laminin (Fig. 4R-U'), a component of the basement membrane. Laminins have been associated with myocardial differentiation and with regulating the sarcolemmal properties (Derrick et al., 2021a; Oliviero et al., 2000; Wang et al., 2019; Wang et al., 2006; Yarnitzky and Volk, 1995). At 5 dpf, in the hearts of control fish (n=5) we observed clear anti-Laminin staining at the basal and lateral domains of cardiomyocytes (Fig. 4R-S'), which correlates with previous observations (Derrick et al., 2021b; Oliviero et al., 2000). Laminin expression levels were severely reduced in *wt1b* overexpression hearts (n=5), with no Laminin observed in the lateral domains of the cardiomyocytes (Fig. 4T-U'). Thus, the observed reduced levels of Laminin and its impaired deposition upon *wt1b* overexpression point towards an improper basal domain of cardiomyocytes. Taken together, our observations indicate that cardiomyocyte apicobasal polarization may be disrupted upon *wt1b* overexpression.

Overexpression of *wt1* in cardiomyocytes hinders cell maturation and disrupts its structural organization

The disruptions in cell junctions and cell extrusion that we observed in *wt1b* overexpressing cardiomyocytes led us to question the maturation and general architecture of these cells.

Using whole mount immunofluorescence, we observed reduced MHC staining in *wt1b*-overexpressing hearts, at 1 dpf (n=6), when compared to controls (n=4) (Fig.

5A-C'). The reduction of MHC staining was specific to the heart, as it was not observed in the skeletal muscle of the myotome (n=6) (Fig. 5D). Although at 6 dpf we observed an increase in the levels of MHC signal in *wt1b* overexpressing cardiomyocytes, the levels never reach those observed in the control group (Fig. 5E-G). We also analyzed *myl7* mRNA expression levels using whole mount *in situ* hybridization. Consistent with the results obtained using MHC immunostaining, at 3 dpf, *myl7* expression was reduced in *myl7:Gal4;eGFP:UAS:wt1b* (23/25) compared to their single transgenic *eGFP:UAS:wt1b* control siblings (Fig. 5H-I). We reasoned that the reduced levels in MHC and *myl7* staining could be indicative of an impaired maturation of cardiomyocytes. To test this hypothesis, we performed immunofluorescence staining against Alcam, a marker for undifferentiated cardiomyocytes (Hirata et al., 2006; Valente et al., 2019). At 6 dpf, we observed higher Alcam staining levels in hearts overexpressing *wt1b* (n=7) when compared to control hearts (n=6) (Fig. 5J-L).

We next analyzed if sarcomere assembly was impaired in *myl7:Gal4;eGFP:UAS:wt1b* animals. We performed immunofluorescence staining against Actinin, a protein known to be produced in the z line of the sarcomeres (Costa et al., 2002). Qualitative assessment of α -Actinin revealed that not only the levels were lower but also the z-lines were thicker and shorter (Fig. 5M-P') upon myocardial *wt1b* overexpression. Z-line disruption was particularly evident in delaminating cardiomyocytes (Fig. 5O, O'). We next sought to analyze sarcomere structure more in detail using serial block face scanning electron microscopy (SBFSEM) (Fig. 5Q-R' and Movies 4-7). Z-bands were present at the sarcomere boundaries in both groups. While sarcomeres could be easily followed from z-band to z-band in the control heart (Fig. 5Q-Q' and Movie 5), this was not possible in *wt1b* overexpressing hearts (Fig. 5R-R' and Movie 7). A further ultrastructural defect we observed in the *wt1b* overexpression heart was the presence of large intercellular spaces of extracellular matrix, between cardiomyocytes, the epicardium, and endocardium. Moreover, while the control heart revealed a clearly visible basement membrane between the epicardium and the myocardium as well the endocardium and myocardium (dark black line), this structure was not always visible in the *wt1b*-overexpressing heart (Fig. 5Q,R and Movies 4 and 6). This observation correlates with the impairment in Laminin staining reported in *wt1b*-overexpressing cardiomyocytes (Fig. 4R-U').

As we saw that cardiomyocyte structure and maturation were disrupted, we decided to evaluate cardiac performance. We performed *in vivo* imaging and analyzed different parameters for heart function in *myl7:Gal4;eGFP:UAS:wt1b* and *myl7:Gal4;eGFP:UAS:RFP* larvae (Fig. S5; n=14). *myl7:Gal4;eGFP:UAS:wt1b* ventricles presented a reduced stroke volume at 2 dpf (0.11 ± 0.04 nl vs 0.04 ± 0.03 nl) and this impairment did not recover at 5 dpf (0.39 ± 0.17 nl vs 0.22 ± 0.08 nl) (Fig. S5B). We next analyzed the heart rate. Although at 2 dpf we could not detect changes in heart rate (114 ± 8 beats per min (bpm) vs 119 ± 8 bpm) we observed a significant decrease heart frequency at 5 dpf upon *wt1b* overexpression (166 ± 13 bpm vs 141 ± 9 bpm) (Fig. S5C). At 2 dpf, the ejection fraction did also not significantly change between both groups (43 ± 14 % vs 51 ± 8 %). However, at 5 dpf there was a clear reduction in the ejection fraction of the atrium in *wt1b* overexpressing hearts compared to controls (55 ± 8 % vs 41 ± 12 %). In contrast, the ventricular ejection fraction was initially significantly reduced at 2 dpf in *wt1b* overexpressing embryos (48 ± 13 % vs 35 ± 13 %) but recovered at 5 dpf (50 ± 8 % vs 49 ± 8 %) (Fig. S5D). The loss of cardiac function suggests that *wt1b* overexpression led to heart failure, as on average only 28% of *myl7:Gal4;eGFP:UAS:wt1b* larvae survived past 6 dpf (of a total of 600 embryos from 6 independent experiments).

Altogether, our findings indicate that sustained expression of *wt1b* in cardiomyocytes impaired cardiomyocyte maturation including cardiomyocyte sarcomere assembly and the extracellular matrix and ultimately disrupting heart function and reducing survival.

***wt1b* overexpression in cardiomyocytes results in reduced chromatin accessibility at loci related to myocardial maturation**

Seeing that *wt1b* overexpression in cardiomyocytes induced several cardiac malformations and caused a phenotypic change in some cells, we decided to explore how the sustained expression of this transcription factor was affecting chromatin accessibility. To this purpose, we performed Assay for Transposase-Accessible Chromatin sequencing (ATAC-seq) (Buenrostro et al., 2013) in 5 dpf, FAC sorted GFP⁺ cells from either the *myl7:Gal4;eGFP:UAS:RFP* control or *myl7:Gal4;eGFP:UAS:wt1b* larvae (Fig. 6A). We identified 1452 differential peaks in *wt1b* overexpressing cardiomyocytes, of which almost all, except for 14 peaks, showed reduced chromatin accessibility (Fig. 6B and Data 1). Most of the differential

accessible regions were located close to promoter regions (38.87%), in introns (30.37%) or in distal intergenic regions (26.14%) (Fig. 6C). We performed Gene Ontology (GO) analysis for the genes lying near the differentially accessible regions. From the top 25 Biological Pathways that had reduced accessibility of regions close to genes associated with these pathways (Fig. S6), five of them account for muscle development (Fig. 6D and Data 2). Of the top 25 Cellular Component pathways (Fig. S6) we found some to be involved in “actin cytoskeleton”, “basolateral plasma membrane”, “apical part of the cells”, “contractile fiber” or “myofibril” (Fig. 6E and Data 2). From the top 25 Molecular Function pathways (Fig. S6) five of them are directly implicated in transcription regulation and another four in cytoskeleton formation and cell adhesion, such as “actin binding”, “actin-filament binding”, “cell adhesion molecule binding” and “beta-catenin binding” (Fig. 6F and Data 2). All of these pathways, which are underrepresented in the *myl7:Gal4;eGFP:UAS:wt1b* samples strongly correlate with the defects observed in hearts overexpressing *wt1b*. To identify potential transcription factors that might be binding to the differentially accessible regions, we performed MEME-Centrismo motif analysis, and found WT1 to be one of the top 5 motifs represented (E-value = 7.8e-5) (Fig. 6G). This motif could be identified in 672 (46.25%) of the differentially accessible regions (3 open and 669 closed) (Fig. 6G'). To further investigate which of the open regulatory regions and their associated genes were potential direct targets of WT1, we compared our ATAC-seq data with WT1 target genes identified in the CHIP-atlas database (Oki et al., 2018). 41% of the regions associated with differential accessibility identified in our ATAC-seq (426, of which only 6 represent regions with open chromatin) were shared with the CHIP-atlas database for WT1. GO analysis of the associated common genes identified pathways similar to those observed previously, suggesting a direct regulation of these pathways by Wt1b (Fig. 6H).

Having seen that overexpression of *wt1b* in cardiomyocytes affected heart development and that these changes correlated with the observed molecular signature, we looked more closely at how the genetic landscape of some of the genes, with associated differentially accessible regions, was affected. We had previously seen that apical cell-cell junctions were disrupted in the hearts of the *myl7:Gal4;eGFP:UAS:wt1b* embryos, including expression and localization of *cdh2*, ZO-1, β -Catenin. In agreement, we observed that putative regulatory regions near

cdh2 and *ctnna* (another core component of adherens junctions) revealed lower accessibility when *wt1b* was overexpressed in cardiomyocytes (Fig. 6I,I'). We also observed lower accessibility in core apicobasal polarity pathway genes (Assémat et al., 2008) such as *pardb6* and *pard3bb* from the apical polarity pathways and *scrib*, *dlg1* and *dlg1l* from the basolateral pathways (Fig. 6J,K and Data 3), supporting a perturbed apicobasal polarity in the *wt1b* overexpression lines. Moreover, we detected that several genes associated with sarcomere assembly such as *e2f3*, *rbfox2* and *rybp* (Gallagher et al., 2011; Henry et al., 2020; King et al., 2008) presented lower chromatin accessibility in *wt1b*-overexpressing cells (Fig. 6L-L' and Supplementary Data 3), which could explain the disrupted sarcomeres observed in the overexpression line (Fig. 5M-R).

In conclusion, ATAC-seq data analysis revealed that *wt1b* overexpression in the heart decreased overall chromatin accessibility associated with key genes involved in cardiomyocyte maturation and structural differentiation, with *Wt1b* likely to directly repress gene expression programs controlling muscle development, cell polarity and actin binding.

DISCUSSION

During myocardial development, cells from the precardiac mesoderm enter the heart tube and contribute to its growth. We found that myocardial expansion at the venous pole occurs through a population of *wt1* positive cells that downregulate *wt1* expression during differentiation. We found that sustained *wt1* activity reduced chromatin accessibility in regulatory regions associated with cardiomyocyte-specific genes and that *wt1* activity in cardiomyocytes can induce their phenotypic switch from myocardial to epicardial-like cells. In a different context, *Wt1* expression has been shown to prevent the activation of a muscle differentiation program (Miyagawa et al., 1998). *Wt1* also impairs the differentiation of embryonic stem cells towards a myocardial lineage (Wagner et al., 2021). These observations suggest that *wt1* might be generally repressing myocyte specification. However, *Wt1* loss of function in cardiomyocytes also impairs heart development (Díaz del Moral et al., 2021) underlining the need for a delicate balance of *Wt1* levels in cardiomyocytes during heart formation.

In this work we report the effect of the overexpression of the –KTS isoform of *Wt1*, that can act as a transcriptional activator or repressor (Toska and Roberts, 2014). Our ATAC-seq results suggest that in cardiac progenitors, *Wt1* might act as a repressor of the myocardial gene program. It will be interesting to further analyze if the +KTS isoform, associated with RNA-binding properties (Toska and Roberts, 2014) would have similar effects on myocardial specification.

While a subset of pericardial cells enters the heart tube, downregulate *wt1* and contribute to myocardial expansion, other cells maintain *wt1* expression and form the proepicardium. During proepicardium formation, *wt1*-positive cells extrude apically from the dorsal pericardial mesothelium giving rise to proepicardial cell clusters that subsequently are transferred to the myocardium forming the epicardium (Andrés-Delgado et al., 2019). Here we find that myocardial *wt1*-positive cells undergo a similar process and delaminate apically from the myocardium. It will be important to further decipher possible parallelisms between these two processes and elucidate the direct role of *wt1* during these cellular rearrangements. *Wt1* participates in the mesothelial-to-mesenchymal transition giving rise to epicardial derived cells (EPDCs) (Martínez-Estrada et al., 2010; von Gise et al., 2011). Moreover, *Wt1* has been suggested to control the retinoic acid (RA) signaling pathway during EPDC formation (Guadix et al., 2011; von Gise et al., 2011). The fact that cardiomyocytes overexpressing *wt1* are relocating to the epicardial layer might indicate that these cells undergo EMT-like processes in response to *wt1* overexpression, a process, which might be mediated by RA. However, the absence of *aldh1a2* expression in the myocardium, prior to delamination suggests that *aldh1a2* expression might be a consequence rather than a cause of apical delamination of *wt1*-expressing cells. Of note, not all eGFP-positive cardiomyocytes undergo delamination. It might thus be possible that not all cardiomyocytes have the capacity to respond to the same extent to *wt1* overexpression. Indeed, in the mouse a small subset of cardiomyocytes has been shown to express *Wt1* and as such, not all cardiomyocytes might be equally sensitive to a change in *Wt1* dosage (Cano et al., 2016; Rudat and Kispert, 2012). Furthermore, this effect is very specific to *wt1* gene function in cardiomyocytes and has not been observed neither by expressing *wt1* in other cardiac cell types nor by overexpressing *tcf21* in cardiomyocytes. Cardiomyocyte extrusion has been

observed in *klf2* and *snai1* mutant zebrafish (Gentile et al., 2021; Rasouli et al., 2018). While in these mutants extruded cardiomyocytes are eliminated, here we report that the extruded *wt1*-positive cells remain on the myocardial surface contributing to the epicardial layer.

Wt1 overexpression in cardiomyocytes had been suggested to trigger a change in cell fate in arrhythmogenic right ventricular cardiomyopathy (ARVC) (Dorn et al., 2018). In this disease, a subset of cardiomyocytes has been proposed to start to express *Wt1* and convert into adipocytes. Interestingly, epicardial fat represents an epicardial derivative (Zangi et al., 2017). Together with our results, this indicates that expression of *Wt1* in cardiomyocytes contributes to a phenotypic change, transforming them into epicardial cells or EPDC-like cells. Genetic profiling of these delaminated cells might provide a better insight into the changes that these cells undergo, to allow for their delamination and phenotypic switch. Previous findings also pointed to the possibility of cell plasticity between epicardium and myocardium whereby epicardial cells could transdifferentiate into cardiomyocytes during development and repair (Smart et al., 2011; Zhou et al., 2008). Here we present evidence of the opposite phenotypic switch, triggered by one single transcription factor. Our work shows that during cardiac development, *wt1a/b* expression is turned off in cardiomyocytes once they enter the heart tube to allow their correct differentiation. Dissecting the regulatory mechanisms controlling *wt1a/b* transcription in cardiomyocyte precursors will further expand our knowledge on the tight spatio-temporal control of heart tube expansion and concomitant cardiomyocyte differentiation.

Materials and Methods

REAGENT/RESOUR	SOURCE	IDENTIFIER
Antibodies		
Rabbit polyclonal anti-Aldh1a2	GeneTex	Cat# GTX124302
Mouse monoclonal anti-CD166 antigen homologue A (neurolin) (Alcama)	DSHB	Cat # ZN-8

Mouse monoclonal anti α -Actinin (sarcomeric) clone EA-53	Sigma Aldrich	Cat # A7811
Mouse monoclonal anti-Caveolin 1	BD biosciences	Cat# 610406
Chicken polyclonal anti-GFP	Aves Labs	Cat# GFP-1010
Mouse monoclonal anti-myosin, sarcomere (MHC)	DSHB	Cat# MF 20, RRID:AB_2147781
Mouse monoclonal anti-ZO-1 (ZO1-1A12)	Invitrogen	Cat # 33-9100
Rabbit anti-Laminin	Sigma Aldrich	Cat # L9393
Mouse monoclonal anti β -Catenin	BD Biosciences	Cat # 610153
Goat anti-Chicken IgY (H+L), Alexa Fluor® 488 conjugate	Thermo Fisher Scientific	Cat # A-11039
Goat anti-Mouse IgG2b, Alexa Fluor® 568 conjugate	Thermo Fisher Scientific	Cat # A-21144
Goat anti-Mouse IgG2b, Alexa Fluor® 647 conjugate	Thermo Fisher Scientific	Cat #A-21242
Goat Anti-Mouse Immunoglobulins/HRP	Dako	Cat # P 0447
Goat anti-Rabbit IgG (H+L) Secondary Antibody, Alexa Fluor® 568 conjugate	Thermo Fisher Scientific	Cat # A-11036

Goat anti-Mouse IgG1, Alexa Fluor® 568 conjugate	Thermo Fisher Scientific	Cat # A-21124
Primers		
Gene	Forward primer	Reverse Primer
<i>Gfp</i>	CAAGATCCGCCACAACAT CG	GACTGGGTGCTCAGGTAG TG
<i>wt1a OE</i>	GAGCCATCCCGGAGGTTA TG	GGTACTCTCCGCACATCCT G
<i>wt1b OE</i>	CCAGGTCTGACCAGCTGA AG	GTGTCTTCAGGTGGTCCG AG
<i>tcf21</i>	ATGTCCACCGGGTCCATC AG	TCAGGAAGCTGTAGTCCC GCA
Chemicals, Peptides, and Recombinant Proteins		
4-hydroxytamoxifen	Sigma Aldrich	Cat#H6278
N-Phenylthiourea (PTU)	Sigma Aldrich	Cat# P7629
Proteinase K	Roche	Cat# 03115801001
Heparin sodium salt from porcine intestinal mucosa	Sigma- Aldrich	Cat# H4784
Formamide	Sigma- Aldrich	Cat# 47670-1L-F
Blocking reagent	Sigma-Aldrich	Cat# 11096176001
Ribonucleic acid from torula yeast	Sigma- Aldrich	Cat# R6625-25G
HBSS (10X), no calcium, no magnesium, no phenol red	Thermo Fisher Scientific	Cat# 14185052
Corning™ 0.05% Trypsin/0.53mM EDTA in HBSS w/o Calcium and Magnesium	Thermo Fisher Scientific	Cat# MT25051CI

Collagenase	Sigma	Cat # C8176
BSA	Sigma	Cat# A3059
Kits		
SMARTer® Ultra™ Low Input RNA for Illumina® Sequencing – HV kit	Takara	Cat# 634828
Agilent's High Sensitivity DNA Kit	Agilent	Cat# 5067-4626
Low Input Library Prep Kit	Illumina	Cat# 634947
Illumina Nextera kit	Illumina	Cat# Fc-121-1030
Illumina Tagment DNA TDE1 Enzyme and Buffer Kits	Illumina	Cat# 20034198
DT® for Illumina Nextera DNA Unique Dual Indexes Set C	Illumina	Cat# 20027215
Bioline MyFi Mix	Meridian Bioscience	Cat# Bio-25050
MinElute PCR Purification Kit	Qiagen	Cat# 28004
AMPure XP	Beckman Coulter	Cat # A63882
Qubit dsDNA HS Assay Kit	Thermo Fisher Scientific	Cat# Q32854
NGS Fragment Kit	Agilent	Cat# DNf-473
Bioline JetSeq library Quantification Lo- ROX kit	Meridian Bioscience	Cat# Bio-68029
NovaSeq XP 2-Lane Kit v1.5	Illumina	Cat# 20043130
NovaSeq 6000 SP Reagent Kit v1.5	Illumina	Cat# 20040719
Software and Algorithms		

Fiji	NIH	SCR_002285
GraphPad Prism 7	GraphPad Software	SCR_002798
Imaris 9.5.1	Bitplane	
MATLAB R2017a	MathWorks	
Specialized Material		
U-shaped glass capillaries	Leica microsystems	Cat # 158007061
MatTek imaging dish, 35 mm	MatTek Corporation	Cat # P35G-0-20-C
Tungsten needles		
Microscopes and Imaging machines		
Nikon SMZ800N	Nikon	
Leica TCS SP8 digital light sheet (DLS)	Leica	
Imager M2	Zeiss	
LSM 880 confocal microscope, with Airyscan	Zeiss	
Quanta FEG 250 SEM (serial block face scanning electron microscope)	FEI	
Experimental Models: Organisms/Strains		
<i>Et(-26.5Hsa.WT1-gata2:eGFP)^{cn1} (epi:eGFP)</i>	(Peralta et al., 2013)	ZDB-ETCONSTRCT-170823-1
<i>Tg(myf7:mRFP)^{ko081g}</i>	(Rohr et al., 2008)	ZDB-TGCONSTRCT-080917-1
<i>Tg(fli1a:Gal4)^{ubs3Tg}</i>	(Herwig et al., 2011)	ZDB-ALT-120113-6
<i>Tg(myf7:Gal4)^{cbg2Tg}</i>	(Mickoleit et al., 2014)	ZDB-TGCONSTRCT-150108-1

<i>Tg(-3.5ubi:loxP-eGFP-loxP-mCherry)^{cz1701}</i>	(Mosimann et al., 2011b)	ZDB-TGCONSTRCT-110124-1
<i>Tg(eGFP:5xUAS:RFP; gcryst:cerulean)^{cn15}</i>	(Sanz-Morejon et al., 2019)	ZDB-TGCONSTRCT-190724-4
<i>Tg(wt1a:CreERT2); cn10Tg</i>	(Sánchez-Iranzo et al., 2018)	ZDB-TGCONSTRCT-170711-9
<i>Tg(-3.5ubi:loxP-EGFP-loxP-mCherry)^{cz1701Tg}</i>	(Mosimann et al., 2011a)	ZDB-ALT-110124-1
<i>Tg(bGl-eGFP:5xUAS:wt1b - bGl; cryaa:eCFP)^{bm4}</i>	This manuscript	ZDB-ALT-200327-14
<i>Tg(bactin2:loxP-DsRed2-loxP-eGFP-T2A-wt1a)^{li21}</i>	This manuscript	N/A
<i>Tg(bGl-eGFP:5xUAS:tcf21 - bGl; cryaa:eCFP)</i>	This manuscript	N/A

Zebrafish husbandry

Experiments were conducted with zebrafish (*Danio rerio*) embryos and adults aged 3–18 months, raised at maximal 5 fish/l. Fish were maintained under the same environmental conditions: 27.5–28°C, with 14 hours of light and 10 hours of dark, 650–700µs/cm, pH 7.5 and 10% of water exchange daily. Experiments were conducted after the approval of the "Amt für Landwirtschaft und Natur" from the Canton of Bern, Switzerland, under the licenses BE95/15 and BE 64/18.

Generation of transgenic lines

To generate the transgenic line *eGFP:UAS:wt1b* and the *eGFP:UAS:tcf21* the RFP fragment from the plasmid used to clone *eGFP:5xUAS:RFP* (Sanz-Morejon et al., 2019) was replaced by either the coding sequence of *wt1b(-KTS)* isoform or of *tcf21*, PCR amplified from 24 hpf and 5 dpf zebrafish embryo cDNA and assembled using

Gibson cloning. The final entire construct is flanked with *Tol2* sites to facilitate transgenesis. In this line, tissue specific expression of Gal4 drives the bidirectional transactivation of the UAS leading to the expression of both *eGFP* and *wt1b(-KTS)* or *tcf21* coding sequence. The full name of these lines is *Tg(bGl-eGFP:5xUAS:wt1b(-KTS)-bGl; cryaa:eCFP)^{brn4}*, *Tg(bGl-eGFP:5xUAS:tcf21)-bGl; cryaa:eCFP)^{brn4}*. The construct *bactin2:loxP-DsRed2-loxP-eGFP-T2A-wt1a* was generated by Gateway cloning (MultiSite Gateway Three-Fragment Vector Construction Kit; Invitrogen). As destination vector pDestTol2pA2 was used. The floxed *DsRed2* cassette was derived from vector *pTol2-EF1alpha-DsRed(floxed)-eGFP* (Hans et al., 2009) and the *wt1a* cDNA was amplified from vector *pCS2P-wt1a* (Bollig et al., 2006). The final construct is flanked with *Tol2* sites to facilitate transgenesis. In the resulting zebrafish line *DsRed* is expressed from the ubiquitous β -actin promoter. After Cre-mediated excision of the STOP cassette both *eGFP* as well as *wt1a* are expressed in a tissue-specific manner. The full name of this line is *Tg(bactin2:loxP-DsRed2-loxP-eGFP-T2A-wt1a)^{y121}*.

Administration of 4-Hydroxytamoxifen (4-OHT)

4-hydroxytamoxifen (4-OHT; Sigma H7904) stock was prepared by dissolving the powder in ethanol, to 10 mM concentration. To aid with the dissolution the stock was heated for 10 minutes (min) at 65°C and then stored at -20°C, protected from the light. 4-OHT was administered at the indicated times, at a final concentration of 10 μ M. For embryos, treatments were performed continuously. Prior to administration, the 10 mM stock was warmed for 10 min at 65 °C (Felker et al., 2016).

In vivo light sheet fluorescence microscopy and retrospective gating

For *in vivo* imaging of the beating zebrafish heart, 2 dpf old embryos were pipetted with melted 1% low melting agarose in E3 medium (about 45°C), containing 0.003% 1-phenyl-2-thiourea (PTU) (*Sigma-Aldrich*) to avoid pigmentation and Tricaine at 0.08 mg/ml, pH 7 to anaesthetize the fish, into a U-shaped glass capillary (Leica microsystems). This U-shaped capillary was mounted in a 35 mm MatTek imaging dish. The dish was filled with E3 medium containing 0.003% PTU and Tricaine at 0.08 mg/ml, pH 7.

Imaging was performed with the Leica TCS SP8 digital light sheet (DLS) microscope. We used a 25x detection objective with NA 0.95 water immersion and a 2.5x illumination objective with a light sheet thickness of 9.4 μm and length of 1197 μm . The total field of view is 295 x 295 μm , fitting the size of the embryonic zebrafish heart, allowing space for sample drift. The images were acquired in XYTZL-acquisition (XY: single optical section, T: time series, Z: serial optical sections, L: looped acquisition) mode for later retrospective gating. The parameters as shown in Table S2 were applied.

The images were saved as single *.lif*-file and transferred to a workstation (*HP-Z series, Dual Intel Xeon e5-2667 v4 3.2 GHz, 256 GB, NVIDIA GeForce GTX 1080 Ti*). A quality check of the data was performed before the data were further processed. The survival of the larva until the end of the acquisition, the sample drift and the degree of bleaching were assessed in the Processor (https://github.com/Alernst/6D_DLS_Beating_Heart%22). The data were only used if the larva survived the acquisition. The single *.lif*-file was converted to XYTC *.tif*-files, using the Converter_6D (https://github.com/Alernst/6D_DLS_Beating_Heart). Each XYTC file was named in the following format “Image_R0000_Z0000” to be recognized for further processing.

Retrospective gating was performed as previously described (Liebling et al., 2005; Liebling et al., 2006; Ohn et al., 2009). The *MATLAB* (R2017a) tool *BeatSync V2.1* was used for retrospective gating (access to the software can be requested from the research group of Michael Liebling). The settings for re-synchronization in the BeatSync software were “*Normalized mutual information*”, “*Recursive Z-alignment*” and “*Nearest-neighbor interpolation*”. One entire heart cycle was re-synchronized in 3D. After re-synchronization, a 3D time lapse of a virtually still heart was created, using the Fiji (Schindelin et al., 2012) tool *Make_timelapse* (https://github.com/Alernst/Make_timelapse) using the *Make_timelapse Fiji* plugin. The time lapse was represented as maximum intensity projection or individual optical slices.

SMARTer-seq

Dorsal pericardium, proepicardium and heart-tube were manually dissected, with tungsten needles, from 60 hpf *epi:eGFP;myl7:mRFP* zebrafish larvae. A minimum of 10 of each tissue/organ were collected for each sample in ice cold PBS. Cells were centrifuged for 7 minutes at 250 g. The excess liquid was removed, and the cells were stored at -80°C until further use. RNA was directly transformed and amplified into cDNA from the lysed tissue using the SMARTer® Ultra™ Low Input RNA for Illumina® Sequencing – HV kit. cDNA quality control was verified using the Agilent 2200 BioAnalyzer and the High Sensitivity DNA Chip from Agilent's High Sensitivity DNA Kit. Next, 50 ng of amplified cDNA were fragmented with the Covaris E220 (Covaris) and used for preparing sequencing libraries using the TruSeq RNA Sample Prep Kit v2 kit (Illumina), starting from the end repair step. Finally, the size of the libraries was checked using the Agilent 2200 Tape Station DNA 1000 and the concentration was determined using the Qubit® fluorometer (Thermo Fisher Scientific). Libraries were sequenced on a HiSeq 2500 (Illumina) to generate 60 bases single reads. FastQ files were obtained using CASAVA v1.8 software (Illumina). NGS experiments were performed in the Genomics Unit of the CNIC.

SMARTer-seq analysis

All bioinformatics analysis were performed using bash scripts or R statistical software. Quality check of the samples was performed using FASTQC and reports summarized using MultiQC (Andrew, 2010; Ewels et al., 2016). Adapters from the fastq files were trimmed using fastp software (Chen et al., 2019). Reads were aligned to GRCz11 danRer11 v102 assembly from Ensembl using STAR (Yates et al., 2020). The reads were summarized using featureCounts (Liao et al., 2014). The counts data were imported to Deseq2 and genes who had expression across all samples (rowSums) greater than or equal to 10 were kept ensuring the reliable expression estimates (Love et al., 2014). After evaluation of the PCA, one of the samples from the heart tube was determined as an outlier and removed from the downstream analysis. The differential expression analysis was performed using 'ashr' LFC Shrikange (Stephens, 2017). A gene was considered as significant if the p adjusted value was <0.05. The plots were plotted using ggplot2 (Wickam, 2016).

Immunofluorescence

Whole mount immunofluorescence on embryos was done as previously described (Sanz-Morejon et al., 2019). Shortly, embryos were fixed over-night, at 4 °C in 4% paraformaldehyde (PFA) (EMS, 15710). Then they were washed with PBS-Tween20 (0.1%) and permeabilized for 30 to 60 min with PBS-TritonX100 (0.5%), depending on the stage and the antibody used. Permeabilization was followed by blocking for 2 hours with histoblock (5% BSA, 5% goat serum, 20mM MgCl₂ in PBS). Afterwards, embryos were incubated overnight, at 4 °C, with the primary antibodies, in 5%BSA. The next day embryos were washed with PBS-Tween20 (0.1%) followed by and overnight incubation in the secondary antibodies, at 4 °C, in 5% BSA. Finally, embryos were washed with PBS-Tween20 (0.1%) and a nuclear counterstain with DAPI (Merck, 1246530100) 1:1000 was done.

Immunofluorescence on paraffin sections was performed as previously described (Gonzalez-Rosa et al., 2011). Briefly, paraffin sections were dewaxed and rehydrated through a series of ethanol incubations, as previously described for histological staining. Afterwards, epitope was recovered by boiling the samples in 10mM citrate buffer, pH 6, for 20 min. Next the same procedure was applied as described above for whole mount immunofluorescence.

The following antibodies were used: primary antibodies - anti-eGFP (Aves, eGFP-1010) was at 1:300, anti-Myosin Heavy Chain at 1:50 (DSHB Iowa Hybridoma Bank, MF20), anti- Aldh1a2 at 1:100 (Gene Tex), anti-Alcama at 1:100 (DSHB Iowa Hybridoma Bank, Zn-8), anti- α -actinin at 1:200 (Sigma Aldrich), anti-Caveolin 1 at 1:100 (BD Biosciences), anti-ZO1 at 1:200 (Invitrogen), anti-Laminin at 1:20 (Sigma) and anti- β -Catenin at 1:100 (BD Biosciences). Secondary antibodies were Alexa Fluor 488, 568, 647 (Life Technologies) at 1:250 and biotin anti-rabbit (Jackson Immuno Research, 111-066-003) followed by StreptavidinCy3 or Cy5 conjugate (Molecular Probes, SA1010 and SA1011) at 1:250.

qRT-PCR assay

Hearts from *Tg(eGFP:5xUAS:wt1bOE-KTS;myl7:Gal4)* and *Tg(eGFP:5xUAS:RFP;myl7:Gal4)* were extracted at 40 dpf. Ventricle, atrium and bulbus arteriosus were manually dissected and stored separately in pools of 5. For each sample, between 3 biological replicates were collected. *Tg(eGFP:UAS:tcf21; -1.5hsp70l:GAL4)* embryos heat shocked at 24 hpf and collected in pools of 50 embryos at 48 hpf for RNA

extraction. Each pool of embryos represented a biological replicate. A total of 4 biological replicates was used for each condition. Total RNA was extracted by using TRI Reagent (Sigma-Aldrich; Cat-No. T9424) according to the manufacturer's recommendations. Afterwards, a total of 200 ng of total RNA was reverse-transcribed into cDNA using High Capacity cDNA Archive Kit (Invitrogen Life Technologies; Cat-No. 4374966). Quantitative PCR (qPCR) was performed in a 7900HT Fast real-time PCR system (Applied Biosystems). qPCR was done using Power Up SYBR Green Master Mix (Applied Biosystems, A25742).

PCR program was run as follows: initial denaturation step was done for 30 s at 95°C, followed by 40 cycles at 95°C for 5 s and 60°C for 30 s. To calculate the relative index of gene expression, we employed the $2^{-\Delta\Delta C_t}$ method, using *e1f2a* expression for normalization.

Double in situ hybridization and immunohistochemistry on paraffin sections

In situ hybridization on paraffin sections was done as follows: paraffin sections were dewaxed and rehydrated through a series of ethanol incubations. Sections were then refixed with 4% PFA at room temperature for 20 min. Afterwards they were washed with PBS and the tissue was permeabilized by incubating the slides with 10 µg/ml of Protease K, for 10 min. at 37°C. Afterwards, slides were washed with PBS and briefly refixed with 4% PFA. The tissue was then incubated for 10 min with triethanolamine 0.1M, pH8 and 0.25% acetic anhydride. After washing the slides with PBS and RNase free water the slides were incubated for 3 hours with pre-hybridization buffer (50% formamide, 5X SSC pH 5.5, 0.1X Denhardt's, 0.1% Tween20, 0.1% CHAPs and 0.05mg/ml tRNA), at 65°C. Afterwards, pre-hybridization buffer was replaced with hybridization buffer (pre-hybridization buffer with mRNA probe). Slides were left to incubate with hybridization buffer overnight at 65°C. The next day, slides were washed twice with post-hybridization buffer I (50% formamide, 5X SSC pH 5.5 and 1% SDS) and 2 times with post-hybridization buffer II (50% formamide, 2X SSC pH 5.5 and 0.2% SDS). Each wash was done for 30 min at 65°C. Slides were then washed another 3 times with maleic acid buffer (MABT) and then incubated for 1 hour blocking solution (2% fetal bovine serum, heat inactivated, and 1% blocking reagent, in MABT). Tissue was incubated overnight at 4°C with anti-DIG antibody in blocking solution at 1:2000. Finally, sections were thoroughly washed with MABT and incubated in alkaline phosphatase buffer (AP buffer, NaCl 0.1M, MgCl₂ 0.05M, 10%

Tri-HCL pH 9.5). Finally, colorimetric assay was performed using BM purple. After the desired staining was achieved, slides were washed with PBS and fixed with 4% PFA, before mounting them with 50% glycerol and imaged using a Zeiss Imager M2, with and Olympus UC50 camera.

After imaging sections were washed and further permeabilized with PBS with 0.5% TritonX-100. Then they were incubated for 2 hours with 5% BSA at room temperature and incubated with primary antibody, chicken anti-GFP (1:300 in 5% BSA) overnight at 4°C. The next day slides were washed in PBS-0.1% Tween20 and incubated for one hour at room temperature with secondary antibody anti-chicken-HRP. Signal was obtained by incubating slides with DAB solution for 30 seconds at room temperature. The reaction was stopped with water. Slides were then mounted in 50% glycerol and imaged.

Whole mount in situ hybridization

Whole mount in situ hybridization was performed as described (Woltering et al., 2009), with some minor adaptations. Embryos were selected at 24 hpf and 3 dpf for eGFP expression. After fixation, the embryos were washed with PBS and gradually dehydrated through a methanol series. Embryos were stored in 100% methanol for a minimum of 2 hours, at -20°C. Afterwards, the embryos were rehydrated and permeabilized with proteinase K (10 µg/ml in TBST) at 37°C. Incubation times were adjusted according to the stage of the embryos (24 hpf, 10 min and 72 hpf, 20 min). This was followed by a 20 min incubation in 0.1M triethanolamine (pH 8), with 25 µl/ml acetic anhydride.

After 4 hours of pre-hybridization, at 68°C, myl7 riboprobe was diluted in pre hybridization solution, at a concentration of 300 ng/ml. The embryos were incubated with the riboprobe overnight, at 68°C. The following day, the riboprobe was removed and the embryos were incubated twice for 30 min with post hybridization solution at 68°C. Embryos were then incubated with blocking buffer, freshly prepared, and afterwards with anti-DIG antibody (in blocking solution), at 1:4000, overnight, at 4°C. The embryos were then washed extensively with Maleic acid buffer (150 mM maleic acid pH 7.5, 300 mM NaCl, 0.1% Tween 20). Finally, the embryos were transferred to a 6-well plate and pre-incubated with AP-buffer (0.1M Tris base pH 9.5, 0.1 M NaCl, 1 mM MgCl₂, 0.1% Tween 20) and then incubated with BM-purple, at room temperature. As soon as color was visible in the heart of either group

(overexpression or control), the staining was stopped in both groups by adding TBST and embryos were re-fixed in 4% PFA.

Using a microscope, we could obtain pictures of the hearts of the embryos. For image acquisition, embryos were mounted on 3% methylcellulose for ease of orientation. Embryos were positioned so that most of the heart could be observed in a single plane.

Images were acquired with a Nikon SMZ800N stereomicroscope. Illumination conditions and acquisition parameters were maintained for all embryos.

Serial block face scanning electron microscopy

Zebrafish embryos at 5 dpf were euthanised with an 0.048 % of tricaine and immediately fixed with 2.5% glutaraldehyde with 0.15M cacodylate buffer and 2mM CaCl_2 , pH 7.4. Embryos were then processed for serial block face scanning electron microscopy as previously described (Odriozola et al., 2017). Briefly we proceed as follows: samples were rinsed 3 times in ice-cold 0.15 M Na-cacodylate for 5 min.

They were then incubated in 0.15 M Na-cacodylate solution containing 2% OsO_4 and 1.5% potassium ferrocyanide for 45 min, at room temperature, and for 15 min in a water bath, at 50 °C. Samples were rinsed 3 times for 5 min in water. They were then incubated with 0.64 M pyrogallol for 15 min at room temperature, for 5 min in a water bath at 50 °C, and subsequently rinsed with water. The embryos were incubated in 2% OsO_4 for 22 min at room temperature and 8 min in a water bath at 50°C.

Afterwards they were again rinsed in water (3 times 5 min) and incubated overnight in a solution of 0.15 M gadolinium acetate (LFG Distribution, Lyon, France) and 0.15 M samarium acetate (LFG Distribution) pH 7.0. The next day the embryos were rinsed 3x5 min with water and incubated in 1% Walton's lead aspartate (Walton, 1979) at 60 °C for 30 min and rinsed with water (3x 5 min).

After staining, the samples were dehydrated in a graded ethanol series (20%, 50%, 70%, 90%, 100%, 100%) at 4°C, each step lasting 5 min. They were then infiltrated with Durcupan resin mixed with ethanol at ratios of 1:3 (v/v), 1:1, and 3:1, each step lasting 2 h. The embryos were left overnight to infiltrate with Durcupan. The next day, samples were transferred to fresh Durcupan and the resin was polymerized for 3 days at 60 °C. Sample blocks were mounted on aluminum pins (Gatan, Pleasanton, CA, USA) with a conductive epoxy glue (CW2400, Circuitworks, Kennesaw, GA, USA). Care was taken to have osmicated material directly exposed at the block

surface in contact with the glue to reduce specimen charging under the electron beam. Pyramids with a surface of approximately $500 \times 500 \mu\text{m}^2$ were trimmed with a razor blade.

Three-dimensional (3D) ultrastructural images were produced by serial block face scanning electron microscopy (SBFSEM) on a Quanta FEG 250 SEM (FEI, Eindhoven, The Netherlands) equipped with a 3View2XP in situ ultramicrotome (Gatan). Images were acquired in low vacuum mode (40 mPa), except where indicated otherwise. Acceleration voltage was 5 kV and pixel dwell time was set to 2 μs . Image acquisition was done with a back scattered electron detector optimized for SBFSEM (Gatan). Image stack were aligned, normalized, and denoised by non-linear anisotropic diffusion in IMOD (Kremer et al., 1996). Each field of view consisted of 8192×8192 pixels with a dimension of 6 nm/pixel in x-y and 50-150 nm in z direction. Final image montage was done in Fiji.

Embryonic heart function analysis

Heartbeat analysis was performed by assessing the following parameters: degree of rhythmic beating as Root Mean Square of Successive Differences (RMSSD) (Collins et al., 2019); stroke volume (SV - difference between diastolic and systolic volume); ejection fraction (EF - difference between diastolic and systolic volume relative to the diastolic size); cardiac output (CO - SV multiplied by heart rate); and diastolic volume, and heart rate as described (DeGroff, 2002; Yalcin et al., 2017)

We recorded 300 frames of the beating heart in the GFP channel in *Tg(myl7:Gal4; eGFP:UAS:wt1b)* and *Tg(myl7:Gal4; eGFP:UAS:RFP)* at 2 dpf and 5 dpf using the fluorescence stereo microscope Nikon SMZ25 (SHR Plan apo 1x objective, 10x zoom, 2880×2048 pixel, $0.44 \mu\text{m}/\text{pixel}$, 17 frames/s).

For the analysis of heart function, we defined the volume of the heart, which is calculated by measuring the long diameter (D_L) and the short diameter (D_S).

$$Volume (nl) = \frac{1}{6} \times \pi \times D_L \times D_S^2$$

The maximal and minimal volume of the ventricle and atrium were measured, to calculate end-diastolic volume (EDV) and end-systolic volume (ESV). The mean EDV and ESV of two heart cycles per fish were averaged to calculate the SV.

$$SV (nl/beat) = EDV - ESV$$

The EF was calculated by dividing the SV through the EDV and converted to a percentage.

$$EF (\%) = \frac{(EDV-ESV)}{EDV} \times 100 = \frac{SV}{EDV} \times 100$$

We developed the FIJI plugin *Heart beat analysis* to sequentially process all images in a folder and guide the user through each manual step of the analysis. The manual steps are (1) find the two diastolic and systolic states of the heart, (2) adjust a line to D_L and D_S and (3) draw one line at the border of the ventricle. The plugin *Heart beat analysis* opens subsets of the data (100 frames and only green channel per fish from the .nd2 RGB file), applies a Gaussian blur filter (10 px), indicates which manual step to perform, calculates the HR by detecting maxima in a kymograph and subsequently saves all kymograph images as .tiff, results as .csv, all lines as .zip in ROI sets.

To calculate the RMSSD we measured the temporal distance between 12-15 cardiac cycles using instead of a subset of 100 frames all 300 frames from the above-described data. The temporal distances between cardiac cycles were measured using the FIJI plugin *RMSSD* (Collins et al., 2019), two line were drawn crossing one side of the cardiac wall of V and AT. Subsequently, kymographs were generated. The correctness of detected maxima in the kymograph was supervised. All intermediate images and ROIs were saved. The locations of each intensity maximum in the kymograph were exported as .csv-file. A Jupyter-notebook (Kluyver et al., 2016) was created to calculate the time between two cardiac cycles ($R - R$; time of cardiac cycle, R ; current cycle, i ; next cycle, $i+1$) and variability of these time differences between all frames (total frames, N) as RMSSD.

$$RMSSD (ms) = \sqrt{\frac{1}{N-1} \left(\sum_{i=1}^{N-1} ((R - R)_{i+1} - (R - R)_i)^2 \right)}$$

FAC sorting

myl7:Gal;eGFP:UAS:RFP and *myl7:Gal;eGFP:UAS:wt1b* embryos at 5 dpf were used to obtain GFP+ heart cells. The heart region of these embryos was manually dissected and placed in Ringer's solution. Afterwards the tissue was briefly centrifuged in a tabletop centrifuge and the Ringer's solution was replaced by a mix

of 20mg/ml collagenase in 0.05% trypsin. The samples were incubated at 32°C for 25 minutes. Every 5 minutes this mixture was gently mixed. The tissue was visually inspected for dissociation. After cell disaggregation the reaction was stopped with Hanks's solution (1xHBS, 10mM Hepes and 0.25%BSA). The homogenized samples were centrifuged at 250g for 10 minutes and re-suspended in Hank's solution. The cells were then passed through a 40 µm filter, centrifuged again for 10 minutes at 400g and re-suspended in 50 µl of Hank's solution for FAC sorting. Dead cells were marked with 7-aminoactinomycin D (Invitrogen) and discarded. Cells were FAC sorted into Hank's solution, on a MoFlo astrios EQ (Beckman Coulter) and analyzed for forward and side scatter, as well as eGFP fluorescence. Between 1200 and 1500 cells per sample were sorted for ATAC-seq.

ATAC-seq

FAC sorted GFP⁺ cells were gently centrifuged, and Hank's solution was replaced by lysis buffer (10mM tris-HCL, pH 7.4, 10mM NaCl, 3mM MgCl₂, 0.1% IGEPAL CA-630). Cells were immediately centrifuged at 500 g for 10 minutes at 4°C. The supernatant was discarded and replaced with the transposition reaction mix (Tn5 in TD buffer) for tagmentation, and incubated at 37°C for 30min. Afterwards, 500mM of EDTA was used for quenching. The solution was incubated for 30 minutes at 50°C. MgCl₂ was added to a final concentration of 45mM. Samples were stored at 4°C before proceeding with PCR amplification. For PCR amplification we used 1.25µl IDT® for Illumina Nextera DNA Unique Dual Indexes Set C, which contains two indexes premixed and 25 µL of Bioline MyFi Mix. This is in the place of the NEB Next HiFi PCR mix in your protocol. We performed the PCR as outlined. For PCR amplification 15 cycles were used due to the reduced amount of material. The amplified library was purified using the Qiagen PCR purification MinElute kit. This was followed by a 1 x volume AMPure XP bead-based clean-up according to manufacturer's guidelines. The resulting libraries were evaluated for quantity and quality using a Thermo Fisher Scientific Qubit 4.0 fluorometer with the Qubit dsDNA HS Assay Kit and an Advanced Analytical Fragment Analyzer System using a Fragment Analyzer NGS Fragment Kit, respectively.

The ATAC-Seq libraries were further quantified by qPCR using a Bioline JetSeq library Quantification Lo-ROX kit according to their guidelines. The libraries were pooled equimolar and further cleaned using AMPure XP beads as described above. The library pool was then again assessed for quantity and quality using fluorometry and capillary electrophoresis as described above.

The pool was loaded at 150pM using an XP workflow into one lane of a NovaSeq 600 SP with NovaSeq XP 2-Lane Kit v1.5. The libraries were sequenced paired end on an Illumina NovaSeq 6000 sequencer using a NovaSeq 6000 SP Reagent Kit v1.5. An average of 56 million reads/library were obtained. The quality of the sequencing runs was assessed using Illumina Sequencing Analysis Viewer and all base call files were demultiplexed and converted into FASTQ files using Illumina bcl2fastq conversion software v2.20. ATAC-seq experiments were performed in collaboration with the Genomics Unit of the University of Bern.

ATAC-seq Data Analysis

All bioinformatics analysis were performed using bash scripts or R statistical software. Quality check of the samples was performed using FASTQC and reports summarized using MultiQC (Andrew, 2010; Ewels et al., 2016). Adapters from the fastq files were trimmed using trimmomatic software (Bolger et al., 2014). Reads were aligned using bowtie2 (Langmead and Salzberg, 2012; Langmead et al., 2019) to GRCz11 danRer11 v102 assembly from Ensembl (Yates et al., 2020) with flags `--very-sensitive`. Paired-end reads were used for downstream analysis. The files were then converted to bam, downsampled to the lowest counts, indexed and the mitochondrial chromosome was removed using samtools (Danecek et al., 2021; Li et al., 2009). Duplicates were removed using Picard tools (2019). The samples were processed to select for unique reads using samtools (Danecek et al., 2021; Li et al., 2009). The peaks were identified using Genrich in ATACSeq mode and zebrafish genome size (Gaspar, 2018). The zebrafish genome size was estimated using faCount script from public utilities from UCSC (Kent et al., 2002).

To analyze the differential accessible regions, we used DiffBind using background and DeSeq2 normalization and a cutoff threshold of $p < 0.05$. To annotate the peaks, we used ChIPSeeker (Yu et al., 2015). We used the GRCz11 danRer11 v102 assembly from Ensembl and transcription start site region as ± 1 kb for annotation.

The annotated genes were then converted to mouse orthologous genes using biomaRt and used for pathway analysis using clusterProfiler (Durinck et al., 2009; Yu et al., 2012). K-means clustering was performed using SeqMINER software using linear enrichment clustering approach with 10 clusters (Ye et al., 2011). The bigwig files to visualize the peaks were made using bamCoverage in deepTools2 (Ramírez et al., 2016). Interactive Genome Viewer was used to visualize the peaks (Robinson et al., 2011).

To identify the transcription factor binding sites, we used the sequences from the differential accessible regions in Centrimo from MEME-suite. We used CIS-BP 2.0 Danio rerio Database to identify the potential zebrafish transcription factors (Bailey and Machanick, 2012; Weirauch et al., 2014).

Imaging and Image processing

Immunofluorescence images were acquired using the Leica TCS SP8 DLS confocal microscopes. For image acquisition of whole mount embryos, larvae were mounted in 1% low melting agarose in a MatTek petri dish. Images were acquired with a 20x water immersion objective. Images were afterwards processed with Fiji software. Figure legends indicate whether a 3D projection is presented or a maximum intensity projection of a reduced number of stacks is shown. For 3D projections, images were first treated with a mean filter, with a radius of 2.0 pixels. Interpolation was also applied when rendering the 3D projections.

To assess the eGFP/mRFP ratio from *in vivo* confocal images, we applied a median filter (3 pixels radius) and measured line profiles from the SV 60 μm into the atrium in 6 sequential Z-planes. The mean intensity along the line profile normalized by the maximum per fluorophore per embryo was calculated, subsequently the ratio for each μm along the line profile was obtained.

For quantification of mean fluorescence intensity first a mean filter with a radius of 2.0 pixels was applied to smoothen the images. Afterwards we did a maximum intensity projection of all the stacks containing the heart. We then delimited the heart and applied an automatic OTSU threshold. Automatic threshold was evaluated independently for each image when necessary minor adjustments were applied. Finally mean fluorescence intensity was calculated.

Semi-quantification of signal intensity for whole mount in situ hybridization was done using Fiji software. First the images were inverted, region of interest (ROI) was defined and used for all images. For each image mean signal was measured in six independent areas: three in the background and three in the stained area.

Measurements were averaged and then background signal subtracted from the signal measured in the stained area. The fold change was calculated and GraphPad was used for statistical analysis.

Statistical Analysis

Statistical analysis was done with GraphPad Prism 7. When data fitted normality parameters, i.e, passed either the D'Agostino-Pearson or the Shapiro-Wilk normality test, an unpaired t-test was used. If this was not the case, the Mann-Whitney non-parametric test was used to compare differences between conditions. In case a statistically significant difference in the standard deviation between conditions was detected, the Unpaired t test with Welch's correction was applied. In case of multiple comparisons, a One-Way ANOVA was applied, followed by Tukey's multicomparisons test. For each presented graph, the type of statistical test applied is stated in the Figure legend.

ACKNOWLEDGEMENTS

We thank Anna Gliwa and Eduardo Diaz for fish husbandry at University of Bern and CNIC, respectively. Microscopes supported by the Microscopy Imaging Center (MIC) at University of Bern were used. We thank Stephan Müller from the FACS Lab of the University of Bern for help with FACS. We thank the Genomics Unit from CNIC for help with SMARTer-seq and Pamela Nicholson and Cátia Coito, from the Genomics Unit of the University of Bern, for help with ATAC-seq. We thank Didier Stainier for sharing the *Tg(myl7:cdh2-tdTomato)^{bns78}* line and Julien Vermot for comments on the manuscript.

COMPETING INTERESTS

The authors declare they have no competing interests.

FUNDING

NM has been funded by SNF grant 320030E-164245 and ERC Consolidator grant 2018 819717. The CNIC is supported by the Instituto de Salud Carlos III (ISCIII), the Ministerio de Ciencia e Innovación (MCIN) and the Pro CNIC Foundation and is a Severo Ochoa Center of Excellence (SEV-2015-0505). Benoît Zuber is supported by SNF grant 179520 and ERA-NET NEURON grant 185536. M.O. was supported by SNF grant PCEFP3_186993.

DATA AVAILABILITY

Zebrafish line information has been deposited at ZFIN.

SMARTer-seq and ATAC-seq raw data has been deposited in GEO Database with the reference GSE179520 and GSE179521 respectively.

Raw data has been deposited to Zenodo DOI 10.5281/zenodo.6077267

AUTHORS CONTRIBUTION

I.M. performed most of the experiments, analyzed data, contributed to interpretation of results, and wrote the manuscript

A.E. contributed to *in vivo* imaging and image processing and quantifications, contributed to writing the manuscript and interpretation of results

P.A. performed sequencing analysis, contributed to writing the manuscript and interpretation of results

A.V. performed immunofluorescence and helped with embryo dissociation for FACS

T.H. performed qPCR and contributed to other experiments

A.S.-M. generated the *eGFP:UAS:wt1b* line

U.N. generated the *Tg(bactin2:loxP-DsRed2-loxP-eGFP-T2A-wt1a)* line

A.O. performed electron Microscopy imaging and image reconstruction

X.L. contributed to histological staining, sectioning and maintenance of lines

L. A.D. contributed to Smart-Seq

B. Z. supervised electron Microscopy imaging and image reconstruction

C.T. performed data analysis not included, but with impact to this work

M.O. provided Fig1 S1 and the interpretation thereof.

F.S helped with ATACseq generation and interpretation thereof

C.E. supervised the generation of the *Tg(bactin2:loxP-DsRed2-loxP-eGFP-T2A-wt1a)*

N.M. conceived the research question to be addressed, contributed to design experiments and interpretation of results, wrote the manuscript, and secured funding.

REFERENCES

- (2019). Picard toolkit. In *Broad Institute, GitHub repository*: Broad Institute.
- Andrés-Delgado, L., Ernst, A., Galardi-Castilla, M., Bazaga, D., Peralta, M., Münch, J., González-Rosa, J. M., Marques, I., Tessadori, F., de la Pompa, J. L., et al.** (2019). Actin dynamics and the Bmp pathway drive apical extrusion of proepicardial cells. *Development (Cambridge, England)* **146**.
- Andrés-Delgado, L., Galardi-Castilla, M., Mercader, N. and Santamaría, L.** (2020). Analysis of wt1a reporter line expression levels during proepicardium formation in the zebrafish. *Histology and histopathology* **35**, 1035-1046.
- Andrew, S.** (2010). FASTQC. A quality control tool for high throughput sequence data. .
- Assémat, E., Bazellières, E., Pallesi-Pocachard, E., Le Bivic, A. and Massey-Harroche, D.** (2008). Polarity complex proteins. *Biochimica et Biophysica Acta (BBA) - Biomembranes* **1778**, 614-630.
- Bailey, T. L. and Machanick, P.** (2012). Inferring direct DNA binding from ChIP-seq. *Nucleic acids research* **40**, e128-e128.
- Bolger, A. M., Lohse, M. and Usadel, B.** (2014). Trimmomatic: a flexible trimmer for Illumina sequence data. *Bioinformatics* **30**, 2114-2120.
- Bollig, F., Mehninger, R., Perner, B., Hartung, C., Schäfer, M., Scharl, M., Volf, J.-N., Winkler, C. and Englert, C.** (2006). Identification and comparative expression analysis of a second wt1 gene in zebrafish. *Developmental Dynamics* **235**, 554-561.
- Bollig, F., Perner, B., Besenbeck, B., Köthe, S., Ebert, C., Taudien, S. and Englert, C.** (2009). A highly conserved retinoic acid responsive element controls wt1a expression in the zebrafish pronephros. *Development (Cambridge, England)* **136**, 2883.
- Buenrostro, J. D., Giresi, P. G., Zaba, L. C., Chang, H. Y. and Greenleaf, W. J.** (2013). Transposition of native chromatin for fast and sensitive epigenomic profiling of open chromatin, DNA-binding proteins and nucleosome position. *Nature Methods* **10**, 1213-1218.
- Cano, E., Carmona, R., Ruiz-Villalba, A., Rojas, A., Chau, Y. Y., Wagner, K. D., Wagner, N., Hastie, N. D., Munoz-Chapuli, R. and Perez-Pomares, J. M.** (2016). Extracardiac septum transversum/proepicardial endothelial cells pattern embryonic coronary arterio-venous connections. *Proceedings of the National Academy of Sciences of the United States of America* **113**, 656-661.
- Chen, D., Zhang, Z., Chen, C., Yao, S., Yang, Q., Li, F., He, X., Ai, C., Wang, M. and Guan, M. X.** (2019). Deletion of Gtpbp3 in zebrafish revealed the hypertrophic cardiomyopathy manifested by aberrant mitochondrial tRNA metabolism. *Nucleic acids research* **47**, 5341-5355.
- Collins, M. M., Ahlberg, G., Hansen, C. V., Guenther, S., Marín-Juez, R., Sokol, A. M., El-Sammak, H., Piesker, J., Hellsten, Y., Olesen, M. S., et al.** (2019). Early sarcomere and metabolic defects in a zebrafish pitx2 cardiac arrhythmia model. *Proceedings of the National Academy of Sciences* **116**, 24115.
- Costa, M. L., Escaleira, R. C., Rodrigues, V. B., Manasfi, M. and Mermelstein, C. S.** (2002). Some distinctive features of zebrafish myogenesis based on unexpected distributions of the muscle cytoskeletal proteins actin, myosin, desmin, α -actinin, troponin and titin. *Mechanisms of Development* **116**, 95-104.

- Danecek, P., Bonfield, J. K., Liddle, J., Marshall, J., Ohan, V., Pollard, M. O., Whitwham, A., Keane, T., McCarthy, S. A., Davies, R. M., et al. (2021). Twelve years of SAMtools and BCFtools. *GigaScience* **10**.
- DeGroff, C. G. (2002). Doppler echocardiography. *Pediatric cardiology* **23**, 307-333.
- Derrick, C. J., Pollitt, E. J. G., Sanchez Sevilla Uruchurtu, A., Hussein, F., Grierson, A. J. and Noël, E. S. (2021a). Lamb1a regulates atrial growth by limiting second heart field addition during zebrafish heart development. *Development (Cambridge, England)* **148**.
- Derrick, C. J., Pollitt, E. J. G., Uruchurtu, A. S. S., Hussein, F. and Noël, E. S. (2021b). Lamb1a regulates atrial growth by limiting excessive, contractility-dependent second heart field addition during zebrafish heart development. *bioRxiv*, 2021.2003.2010.434727.
- Díaz del Moral, S., Barrena, S., Hernández-Torres, F., Aránega, A., Villaescusa, J. M., Gómez Doblas, J. J., Franco, D., Jiménez-Navarro, M., Muñoz-Chápuli, R. and Carmona, R. (2021). Deletion of the Wilms' Tumor Suppressor Gene in the Cardiac Troponin-T Lineage Reveals Novel Functions of WT1 in Heart Development. *Frontiers in Cell and Developmental Biology* **9**, 1847.
- Dorn, T., Kornherr, J., Parrotta, E. I., Zawada, D., Ayetey, H., Santamaria, G., Iop, L., Mastantuono, E., Sinnecker, D., Goedel, A., et al. (2018). Interplay of cell-cell contacts and RhoA/MRTF-A signaling regulates cardiomyocyte identity. *The EMBO journal* **37**.
- Durinck, S., Spellman, P. T., Birney, E. and Huber, W. (2009). Mapping identifiers for the integration of genomic datasets with the R/Bioconductor package biomaRt. *Nature Protocols* **4**, 1184-1191.
- Eisen, J. S. (2020). *The Zebrafish in Biomedical Research. Biology, Husbandry, Diseases, and Research Applications*: Academic Press.
- Ewels, P., Magnusson, M., Lundin, S. and Käller, M. (2016). MultiQC: summarize analysis results for multiple tools and samples in a single report. *Bioinformatics* **32**, 3047-3048.
- Felker, A., Nieuwenhuize, S., Dolbois, A., Blazkova, K., Hess, C., Low, L. W., Burger, S., Samson, N., Carney, T. J., Bartunek, P., et al. (2016). In Vivo Performance and Properties of Tamoxifen Metabolites for CreERT2 Control. *PLoS One* **11**, e0152989.
- Fukuda, R., Gunawan, F., Beisaw, A., Jimenez-Amilburu, V., Maischein, H.-M., Kostin, S., Kawakami, K. and Stainier, D. Y. R. (2017). Proteolysis regulates cardiomyocyte maturation and tissue integration. *Nature Communications* **8**, 14495.
- Gallagher, T. L., Arribere, J. A., Geurts, P. A., Exner, C. R. T., McDonald, K. L., Dill, K. K., Marr, H. L., Adkar, S. S., Garnett, A. T., Amacher, S. L., et al. (2011). Rbfox-regulated alternative splicing is critical for zebrafish cardiac and skeletal muscle functions. *Developmental Biology* **359**, 251-261.
- Gaspar, J. M. (2018). Genrich: Detecting Sites of Genomic Enrichment. GitHub repository. : GitHub.
- Gentile, A., Bensimon-Brito, A., Priya, R., Maischein, H.-M., Piesker, J., Günther, S., Gunawan, F. and Stainier, D. Y. R. (2020). The EMT transcription factor Snai1 maintains myocardial wall integrity by repressing intermediate filament gene expression. *bioRxiv*, 2020.2012.2015.422833.
- Gentile, A., Bensimon-Brito, A., Priya, R., Maischein, H. M., Piesker, J., Guenther, S., Gunawan, F. and Stainier, D. Y. (2021). The EMT transcription factor Snai1 maintains myocardial wall integrity by repressing intermediate filament gene expression. *Elife* **10**.
- Gonzalez-Rosa, J. M., Martin, V., Peralta, M., Torres, M. and Mercader, N. (2011). Extensive scar formation and regression during heart regeneration after cryoinjury in zebrafish. *Development (Cambridge, England)* **138**, 1663-1674.
- Grivas, D., González-Rajal, Á., Guerrero Rodríguez, C., Garcia, R. and de la Pompa, J. L. (2020). Loss of Caveolin-1 and caveolae leads to increased cardiac cell stiffness and functional decline of the adult zebrafish heart. *Scientific reports* **10**, 12816.
- Guadix, J. A., Ruiz-Villalba, A., Lettice, L., Velecela, V., Muñoz-Chápuli, R., Hastie, N. D., Pérez-Pomares, J. M. and Martínez-Estrada, O. M. (2011). Wt1 controls retinoic acid signalling in embryonic epicardium through transcriptional activation of Raldh2. *Development (Cambridge, England)* **138**, 1093.

- Hans, S., Kaslin, J., Freudenreich, D. and Brand, M. (2009). Temporally-controlled site-specific recombination in zebrafish. *PLoS One* **4**, e4640.
- Hastie, N. D. (2017). Wilms' tumour 1 (WT1) in development, homeostasis and disease. *Development (Cambridge, England)* **144**, 2862-2872.
- Henry, S., Szabó, V., Sutus, E. and Purity, M. K. (2020). RYBP is important for cardiac progenitor cell development and sarcomere formation. *PLOS ONE* **15**, e0235922.
- Herwig, L., Blum, Y., Krudewig, A., Ellertsdottir, E., Lenard, A., Belting, H.-G. and Affolter, M. (2011). Distinct Cellular Mechanisms of Blood Vessel Fusion in the Zebrafish Embryo. *Current Biology* **21**, 1942-1948.
- Hirata, H., Murakami, Y., Miyamoto, Y., Tosaka, M., Inoue, K., Nagahashi, A., Jakt, L. M., Asahara, T., Iwata, H., Sawa, Y., et al. (2006). ALCAM (CD166) is a surface marker for early murine cardiomyocytes. *Cells, tissues, organs* **184**, 172-180.
- Huang, W., Zhang, R. and Xu, X. (2009). Myofibrillogenesis in the developing zebrafish heart: A functional study of tnnt2. *Dev Biol* **331**, 237-249.
- Kent, W. J., Sugnet, C. W., Furey, T. S., Roskin, K. M., Pringle, T. H., Zahler, A. M., Haussler and David (2002). The Human Genome Browser at UCSC. *Genome Research* **12**, 996-1006.
- Kikuchi, K., Gupta, V., Wang, J., Holdway, J. E., Wills, A. A., Fang, Y. and Poss, K. D. (2011). tcf21+ epicardial cells adopt non-myocardial fates during zebrafish heart development and regeneration. *Development (Cambridge, England)* **138**, 2895.
- Kikuchi, K., Holdway, J. E., Werdich, A. A., Anderson, R. M., Fang, Y., Egnaczyk, G. F., Evans, T., MacRae, C. A., Stainier, D. Y. R. and Poss, K. D. (2010). Primary contribution to zebrafish heart regeneration by gata4+ cardiomyocytes. *Nature* **464**, 601-605.
- King, J. C., Moskowitz, I. P. G., Burgon, P. G., Ahmad, F., Stone, J. R., Seidman, J. G. and Lees, J. A. (2008). E2F3 plays an essential role in cardiac development and function. *Cell Cycle* **7**, 3775-3780.
- Kluyver, T., Ragan-Kelley, B., Pérez, F., Granger, B., Bussonnier, M., Frederic, J., Kelley, K., Hamrick, J., Grout, J., Corlay, S., et al. (2016). Jupyter Notebooks – a publishing format for reproducible computational workflows. In *20th International Conference on Electronic Publishing (01/01/16)* (eds F. Loizides & B. Schmidt), pp. 87-90: IOS Press.
- Knight, H. G. and Yelon, D. (2016). Utilizing Zebrafish to Understand Second Heart Field Development. In *Etiology and Morphogenesis of Congenital Heart Disease: From Gene Function and Cellular Interaction to Morphology* (ed. T. Nakanishi, R. R. Markwald, H. S. Baldwin, B. B. Keller, D. Srivastava & H. Yamagishi), pp. 193-199. Tokyo: Springer
- Copyright 2016, The Author(s).
- Kremer, J. R., Mastronarde, D. N. and McIntosh, J. R. (1996). Computer Visualization of Three-Dimensional Image Data Using IMOD. *Journal of Structural Biology* **116**, 71-76.
- Langmead, B. and Salzberg, S. L. (2012). Fast gapped-read alignment with Bowtie 2. *Nature Methods* **9**, 357-359.
- Langmead, B., Wilks, C., Antonescu, V. and Charles, R. (2019). Scaling read aligners to hundreds of threads on general-purpose processors. *Bioinformatics* **35**, 421-432.
- Li, H., Handsaker, B., Wysoker, A., Fennell, T., Ruan, J., Homer, N., Marth, G., Abecasis, G., Durbin, R. and Genome Project Data Processing, S. (2009). The Sequence Alignment/Map format and SAMtools. *Bioinformatics* **25**, 2078-2079.
- Liao, Y., Smyth, G. K. and Shi, W. (2014). featureCounts: an efficient general purpose program for assigning sequence reads to genomic features. *Bioinformatics* **30**, 923-930.
- Liebling, M., Forouhar, A. S., Gharib, M., Fraser, S. E. and Dickinson, M. E. (2005). Four-dimensional cardiac imaging in living embryos via postacquisition synchronization of nongated slice sequences. *Journal of biomedical optics* **10**, 054001.
- Liebling, M., Forouhar, A. S., Wolleschensky, R., Zimmermann, B., Ankerhold, R., Fraser, S. E., Gharib, M. and Dickinson, M. E. (2006). Rapid three-dimensional imaging and analysis of the beating embryonic heart reveals functional changes during development. *Developmental dynamics : an official publication of the American Association of Anatomists* **235**, 2940-2948.

- Love, M. I., Huber, W. and Anders, S. (2014). Moderated estimation of fold change and dispersion for RNA-seq data with DESeq2. *Genome Biology* **15**, 550.
- Martínez-Estrada, O. M., Lettice, L. A., Essafi, A., Guadix, J. A., Slight, J., Velecela, V., Hall, E., Reichmann, J., Devenney, P. S., Hohenstein, P., et al. (2010). Wt1 is required for cardiovascular progenitor cell formation through transcriptional control of Snail and E-cadherin. *Nature Genetics* **42**, 89-93.
- Mickoleit, M., Schmid, B., Weber, M., Fahrbach, F. O., Hombach, S., Reischauer, S. and Huisken, J. (2014). High-resolution reconstruction of the beating zebrafish heart. *Nature Methods* **11**, 919-922.
- Miyagawa, K., Kent, J., Moore, A., Charlieu, J. P., Little, M. H., Williamson, K. A., Kelsey, A., Brown, K. W., Hassam, S., Briner, J., et al. (1998). Loss of WT1 function leads to ectopic myogenesis in Wilms' tumour. *Nat Genet* **18**, 15-17.
- Moore, A. W., McInnes, L., Kreidberg, J., Hastie, N. D. and Schedl, A. (1999). YAC complementation shows a requirement for Wt1 in the development of epicardium, adrenal gland and throughout nephrogenesis. *Development (Cambridge, England)* **126**, 1845-1857.
- Mosimann, C., Kaufman, C. K., Li, P., Pugach, E. K., Tamplin, O. J. and Zon, L. I. (2011a). Ubiquitous transgene expression and Cre-based recombination driven by the ubiquitin promoter in zebrafish. *Development (Cambridge, England)* **138**, 169-177.
- Mosimann, C., Kaufman, C. K., Li, P., Pugach, E. K., Tamplin, O. J. and Zon, L. I. (2011b). Ubiquitous transgene expression and Cre-based recombination driven by the ubiquitin promoter in zebrafish. *Development (Cambridge, England)* **138**, 169-177.
- Niederreither, K., Vermot, J., Schuhbaur, B., Chambon, P. and Dollé, P. (2002). Embryonic retinoic acid synthesis is required for forelimb growth and anteroposterior patterning in the mouse. *Development (Cambridge, England)* **129**, 3563.
- Odriozola, A., Llodrá, J., Radecke, J., Rueggsegger, C., Tschanz, S., Saxena, S., Stephan, R. and Zuber, B. (2017). High contrast staining for serial block face scanning electron microscopy without uranyl acetate. *bioRxiv*, 207472.
- Ohn, J., Tsai, H. J. and Liebling, M. (2009). Joint dynamic imaging of morphogenesis and function in the developing heart. *Organogenesis* **5**, 248-255.
- Oki, S., Ohta, T., Shioi, G., Hatanaka, H., Ogasawara, O., Okuda, Y., Kawaji, H., Nakaki, R., Sese, J. and Meno, C. (2018). ChIP-Atlas: a data-mining suite powered by full integration of public ChIP-seq data. *EMBO reports* **19**.
- Oliviero, P., Chassagne, C., Salichon, N., Corbier, A., Hamon, G., Marotte, F., Charlemagne, D., Rappaport, L. and Samuel, J.-L. (2000). Expression of laminin $\alpha 2$ chain during normal and pathological growth of myocardium in rat and human. *Cardiovascular Research* **46**, 346-355.
- Peralta, M., González-Rosa, J. M., Marques, I. J. and Mercader, N. (2014). The Epicardium in the Embryonic and Adult Zebrafish. *J Dev Biol* **2**, 101-116.
- Peralta, M., Steed, E., Harlepp, S., González-Rosa, Juan M., Monduc, F., Ariza-Cosano, A., Cortés, A., Rayón, T., Gómez-Skarmeta, J.-L., Zapata, A., et al. (2013). Heartbeat-Driven Pericardiac Fluid Forces Contribute to Epicardium Morphogenesis. *Current Biology* **23**, 1726-1735.
- Perner, B., Englert, C. and Bollig, F. (2007). The Wilms tumor genes wt1a and wt1b control different steps during formation of the zebrafish pronephros. *Developmental Biology* **309**, 87-96.
- Pestel, J., Ramadass, R., Gauvrit, S., Helker, C., Herzog, W. and Stainier, D. Y. R. (2016). Real-time 3D visualization of cellular rearrangements during cardiac valve formation. *Development (Cambridge, England)* **143**, 2217-2227.
- Phillips, H. M., Rhee, H. J., Murdoch, J. N., Hildreth, V., Peat, J. D., Anderson, R. H., Copp, A. J., Chaudhry, B. and Henderson, D. J. (2007). Disruption of Planar Cell Polarity Signaling Results in Congenital Heart Defects and Cardiomyopathy Attributable to Early Cardiomyocyte Disorganization. *Circulation Research* **101**, 137-145.
- Ramírez, F., Ryan, D. P., Grüning, B., Bhardwaj, V., Kilpert, F., Richter, A. S., Heyne, S., Dündar, F. and Manke, T. (2016). deepTools2: a next generation web server for deep-sequencing data analysis. *Nucleic acids research* **44**, W160-W165.

- Rasouli, S. J., El-Brolosy, M., Tseke, A. T., Bensimon-Brito, A., Ghanbari, P., Maischein, H.-M., Kuenne, C. and Stainier, D. Y. (2018). The flow responsive transcription factor Klf2 is required for myocardial wall integrity by modulating Fgf signaling. *eLife* **7**, e38889.
- Robinson, J. T., Thorvaldsdóttir, H., Winckler, W., Guttman, M., Lander, E. S., Getz, G. and Mesirov, J. P. (2011). Integrative genomics viewer. *Nature Biotechnology* **29**, 24-26.
- Rohr, S., Otten, C. and Abdelilah-Seyfried, S. (2008). Asymmetric Involution of the Myocardial Field Drives Heart Tube Formation in Zebrafish. *Circulation Research* **102**, e12-e19.
- Rudat, C. and Kispert, A. (2012). Wt1 and epicardial fate mapping. *Circ Res* **111**, 165-169.
- Sánchez-Iranzo, H., Galardi-Castilla, M., Sanz-Morejón, A., González-Rosa, J. M., Costa, R., Ernst, A., Sainz de Aja, J., Langa, X. and Mercader, N. (2018). Transient fibrosis resolves via fibroblast inactivation in the regenerating zebrafish heart. *Proceedings of the National Academy of Sciences* **115**, 4188.
- Sanz-Morejon, A., Garcia-Redondo, A. B., Reuter, H., Marques, I. J., Bates, T., Galardi-Castilla, M., Grosse, A., Manig, S., Langa, X., Ernst, A., et al. (2019). Wilms Tumor 1b Expression Defines a Pro-regenerative Macrophage Subtype and Is Required for Organ Regeneration in the Zebrafish. *Cell reports* **28**, 1296-1306.e1296.
- Schindelin, J., Arganda-Carreras, I., Frise, E., Kaynig, V., Longair, M., Pietzsch, T., Preibisch, S., Rueden, C., Saalfeld, S., Schmid, B., et al. (2012). Fiji: an open-source platform for biological-image analysis. *Nature Methods* **9**, 676-682.
- Serluca, F. C. (2008). Development of the proepicardial organ in the zebrafish. *Dev Biol* **315**, 18-27.
- Serluca, F. C. and Fishman, M. C. (2001). Pre-pattern in the pronephric kidney field of zebrafish. *Development (Cambridge, England)* **128**, 2233-2241.
- Sheikh, F., Ross, R. S. and Chen, J. (2009). Cell-cell connection to cardiac disease. *Trends Cardiovasc Med* **19**, 182-190.
- Smart, N., Bollini, S., Dubé, K. N., Vieira, J. M., Zhou, B., Davidson, S., Yellon, D., Riegler, J., Price, A. N., Lythgoe, M. F., et al. (2011). De novo cardiomyocytes from within the activated adult heart after injury. *Nature* **474**, 640-644.
- Stainier, D. Y., Lee, R. K. and Fishman, M. C. (1993). Cardiovascular development in the zebrafish. I. Myocardial fate map and heart tube formation. *Development (Cambridge, England)* **119**, 31-40.
- Stephens, M. (2017). False discovery rates: a new deal. *Biostatistics* **18**, 275-294.
- Stevenson, B. R., Siliciano, J. D., Mooseker, M. S. and Goodenough, D. A. (1986). Identification of ZO-1: a high molecular weight polypeptide associated with the tight junction (zonula occludens) in a variety of epithelia. *The Journal of cell biology* **103**, 755-766.
- Sugimoto, K., Hui, S. P., Sheng, D. Z. and Kikuchi, K. (2017). Dissection of zebrafish shha function using site-specific targeting with a Cre-dependent genetic switch. *eLife* **6**, e24635.
- Toska, E. and Roberts, S. G. (2014). Mechanisms of transcriptional regulation by WT1 (Wilms' tumour 1). *Biochem J* **461**, 15-32.
- Tyser, R. C. V., Ibarra-Soria, X., McDole, K., Arcot Jayaram, S., Godwin, J., van den Brand, T. A. H., Miranda, A. M. A., Scialdone, A., Keller, P. J., Marioni, J. C., et al. (2021). Characterization of a common progenitor pool of the epicardium and myocardium. *Science* **371**, eabb2986.
- Valente, M., Resende, T. P., Nascimento, D. S., Burlen-Defranoux, O., Soares-da-Silva, F., Dupont, B., Cumano, A. and Pinto-do-Ó, P. (2019). Mouse HSA+ immature cardiomyocytes persist in the adult heart and expand after ischemic injury. *PLOS Biology* **17**, e3000335.
- van der Linde, D., Konings, E. E. M., Slager, M. A., Witsenburg, M., Helbing, W. A., Takkenberg, J. J. M. and Roos-Hesselink, J. W. (2011). Birth Prevalence of Congenital Heart Disease Worldwide: A Systematic Review and Meta-Analysis. *Journal of the American College of Cardiology* **58**, 2241-2247.
- van Wijk, B., Gunst, Q. D., Moorman, A. F. M. and van den Hoff, M. J. B. (2012). Cardiac Regeneration from Activated Epicardium. *PLOS ONE* **7**, e44692.

- Vieira, J. M., Howard, S., Villa del Campo, C., Bollini, S., Dubé, K. N., Masters, M., Barnette, D. N., Rohling, M., Sun, X., Hankins, L. E., et al. (2017). BRG1-SWI/SNF-dependent regulation of the Wt1 transcriptional landscape mediates epicardial activity during heart development and disease. *Nature Communications* **8**, 16034.
- von Gise, A., Zhou, B., Honor, L. B., Ma, Q., Petryk, A. and Pu, W. T. (2011). WT1 regulates epicardial epithelial to mesenchymal transition through β -catenin and retinoic acid signaling pathways. *Developmental biology* **356**, 421-431.
- Wagner, N., Ninkov, M., Vukolic, A., Cubukcuoglu Deniz, G., Rassoulzadegan, M., Michiels, J. F. and Wagner, K. D. (2021). Implications of the Wilms' Tumor Suppressor Wt1 in Cardiomyocyte Differentiation. *Int J Mol Sci* **22**.
- Walton, J. (1979). Lead aspartate, an en bloc contrast stain particularly useful for ultrastructural enzymology. *Journal of Histochemistry & Cytochemistry* **27**, 1337-1342.
- Wamstad, J. A., Alexander, J. M., Truty, R. M., Shrikumar, A., Li, F., Eilertson, K. E., Ding, H., Wylie, J. N., Pico, A. R., Capra, J. A., et al. (2012). Dynamic and coordinated epigenetic regulation of developmental transitions in the cardiac lineage. *Cell* **151**, 206-220.
- Wang, D., Wang, Y., Liu, H., Tong, C., Ying, Q., Sachinidis, A., Li, L. and Peng, L. (2019). Laminin promotes differentiation of rat embryonic stem cells into cardiomyocytes by activating the integrin/FAK/PI3K p85 pathway. *Journal of Cellular and Molecular Medicine* **23**, 3629-3640.
- Wang, J., Hoshijima, M., Lam, J., Zhou, Z., Jokiel, A., Dalton, N. D., Hultenby, K., Ruiz-Lozano, P., Ross, J., Tryggvason, K., et al. (2006). Cardiomyopathy Associated with Microcirculation Dysfunction in Laminin α 4 Chain-deficient Mice*. *Journal of Biological Chemistry* **281**, 213-220.
- Weinberger, M., Simoes, F. C., Patient, R., Sauka-Spengler, T. and Riley, P. R. (2020). Functional Heterogeneity within the Developing Zebrafish Epicardium. *Developmental cell* **52**, 574-590.e576.
- Weirauch, Matthew T., Yang, A., Albu, M., Cote, A. G., Montenegro-Montero, A., Drewe, P., Najafabadi, Hamed S., Lambert, Samuel A., Mann, I., Cook, K., et al. (2014). Determination and Inference of Eukaryotic Transcription Factor Sequence Specificity. *Cell* **158**, 1431-1443.
- WHO (2020). World Health Organisation.
- Wickam, H., Navarro, D., Pederson TL (2016). *ggplot2: elegant graphics for data analysis*: Springer.
- Woltering, J. M., Vonk, F. J., Müller, H., Bardine, N., Tuduice, I. L., de Bakker, M. A. G., Knöchel, W., Sirbu, I. O., Durston, A. J. and Richardson, M. K. (2009). Axial patterning in snakes and caecilians: Evidence for an alternative interpretation of the Hox code. *Developmental Biology* **332**, 82-89.
- Yalcin, H. C., Amindari, A., Butcher, J. T., Althani, A. and Yacoub, M. (2017). Heart function and hemodynamic analysis for zebrafish embryos. *Developmental Dynamics* **246**, 868-880.
- Yang, J., Shih, Y.-h. and Xu, X. (2014). Understanding Cardiac Sarcomere Assembly With Zebrafish Genetics. *The Anatomical Record* **297**, 1681-1693.
- Yarnitzky, T. and Volk, T. (1995). Laminin is required for heart, somatic muscles, and gut development in the Drosophila embryo. *Dev Biol* **169**, 609-618.
- Yates, A. D., Achuthan, P., Akanni, W., Allen, J., Allen, J., Alvarez-Jarreta, J., Amode, M. R., Armean, I. M., Azov, A. G., Bennett, R., et al. (2020). Ensembl 2020. *Nucleic acids research* **48**, D682-D688.
- Ye, T., Krebs, A. R., Choukrallah, M.-A., Keime, C., Plewniak, F., Davidson, I. and Tora, L. (2011). seqMINER: an integrated ChIP-seq data interpretation platform. *Nucleic acids research* **39**, e35-e35.
- Yelon, D., Horne, S. A. and Stainier, D. Y. R. (1999). Restricted Expression of Cardiac Myosin Genes Reveals Regulated Aspects of Heart Tube Assembly in Zebrafish. *Developmental Biology* **214**, 23-37.
- Yu, G., Wang, L.-G., Han, Y. and He, Q.-Y. (2012). clusterProfiler: an R Package for Comparing Biological Themes Among Gene Clusters. *OMICS: A Journal of Integrative Biology* **16**, 284-287.

- Yu, G., Wang, L.-G. and He, Q.-Y.** (2015). ChIPseeker: an R/Bioconductor package for ChIP peak annotation, comparison and visualization. *Bioinformatics* **31**, 2382-2383.
- Zangi, L., Oliveira, M. S., Ye, L. Y., Ma, Q., Sultana, N., Hadas, Y., Chepurko, E., Später, D., Zhou, B., Chew, W. L., et al.** (2017). Insulin-Like Growth Factor 1 Receptor-Dependent Pathway Drives Epicardial Adipose Tissue Formation After Myocardial Injury. *Circulation* **135**, 59-72.
- Zhou, B., Honor, L. B., He, H., Ma, Q., Oh, J.-H., Butterfield, C., Lin, R.-Z., Melero-Martin, J. M., Dolmatova, E., Duffy, H. S., et al.** (2011). Adult mouse epicardium modulates myocardial injury by secreting paracrine factors. *The Journal of Clinical Investigation* **121**, 1894-1904.
- Zhou, B., Ma, Q., Rajagopal, S., Wu, S. M., Domian, I., Rivera-Feliciano, J., Jiang, D., von Gise, A., Ikeda, S., Chien, K. R., et al.** (2008). Epicardial progenitors contribute to the cardiomyocyte lineage in the developing heart. *Nature* **454**, 109-113.
- Zihni, C., Mills, C., Matter, K. and Balda, M. S.** (2016). Tight junctions: from simple barriers to multifunctional molecular gates. *Nature Reviews Molecular Cell Biology* **17**, 564-580.

Figures

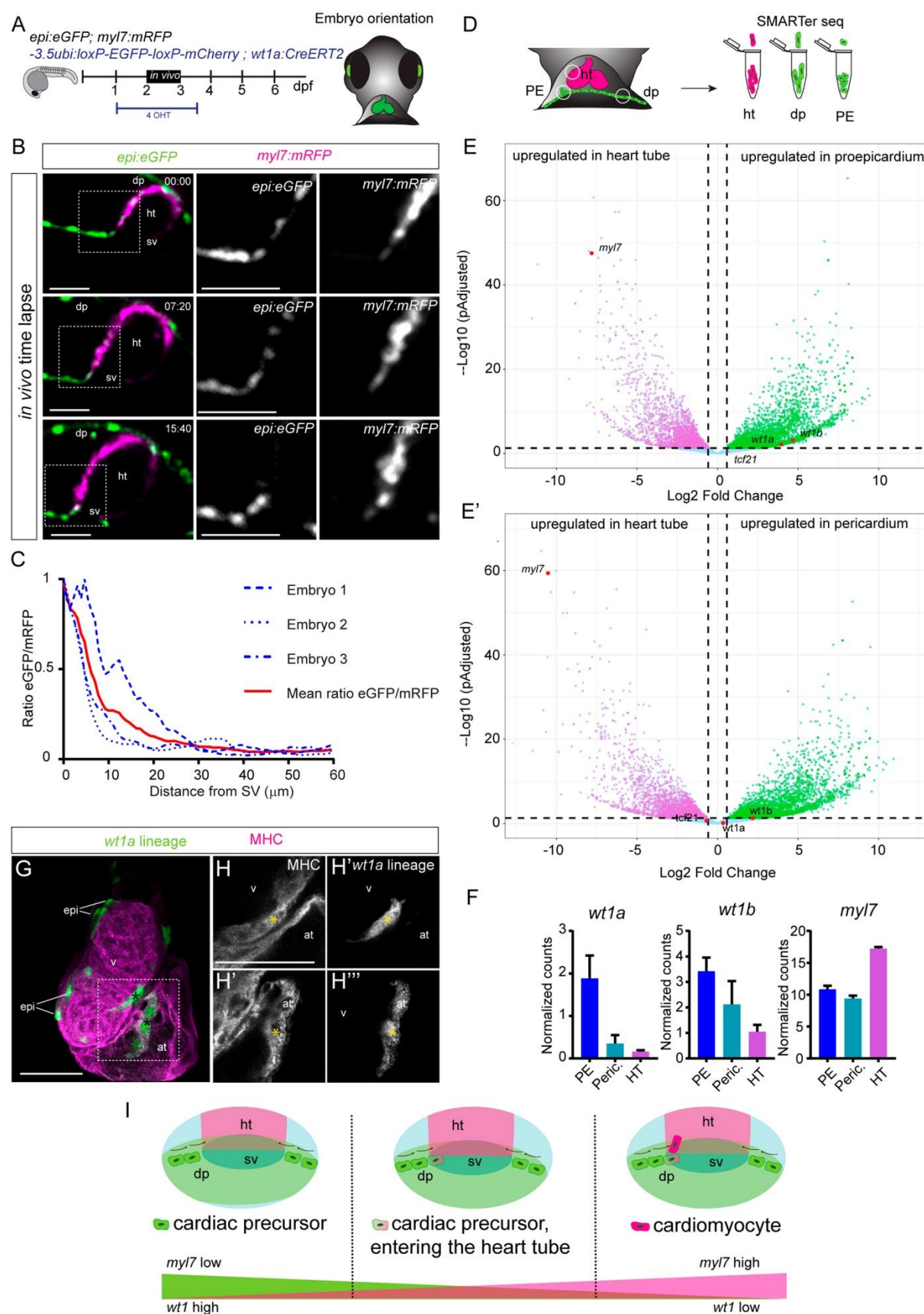


Fig.1. *wt1a* positive cells lose eGFP expression upon entering the heart tube.

- (A) Schematic representation of the *in vivo* imaging of the developing heart tube.
- (B) Time-lapse images of the developing heart tube between 52 and 68 hours post fertilization (hpf) in the double transgenic line *epi:eGFP;myl7:mRFP*. Grey images are single channel zoomed images from the boxes in the merged panels. There is an opposite gradual shift in the expression levels between eGFP and RFP along the time.
- (C) Quantification of the ratio of eGFP and mRFP levels in cells of the heart tube according to the distance to the sinus venosus (SV).
- (D) Schematic representation of tissue dissection for SMARTer-seq of dorsal pericardium, proepicardium and heart tubes of zebrafish embryos.
- (E-E') Volcano plots. Magenta dots indicate upregulated genes in the heart tube. Green dots mark genes upregulated in proepicardium (E) or pericardium (E').
- (F) Quantification of normalized counts for the epicardial marker genes *wt1a* and *wt1b*, and the myocardial gene *myl7*.
- (G-H''') Whole mount immunofluorescence against GFP and Myosin Heavy Chain (MHC) of *wt1a:CreErt2/ubi:switch* zebrafish embryos, recombined between 24 and 96 hpf. Shown is a heart of a 5 days post-fertilization (dpf) embryo. GFP expressing cells mark cells derived from *wt1a* progenitors. (H-H''') are single slice zoomed regions of the boxed region in G. Asterisks indicate cells that co-express GFP and MHC.
- (I) Schematic representation of the downregulation of eGFP and upregulation of mRFP in cardiomyocyte progenitors upon their entry into the heart tube.
- Scale bars: 50 μ m. dp, dorsal pericardium; ht, heart tube; sv, sinus venosus.

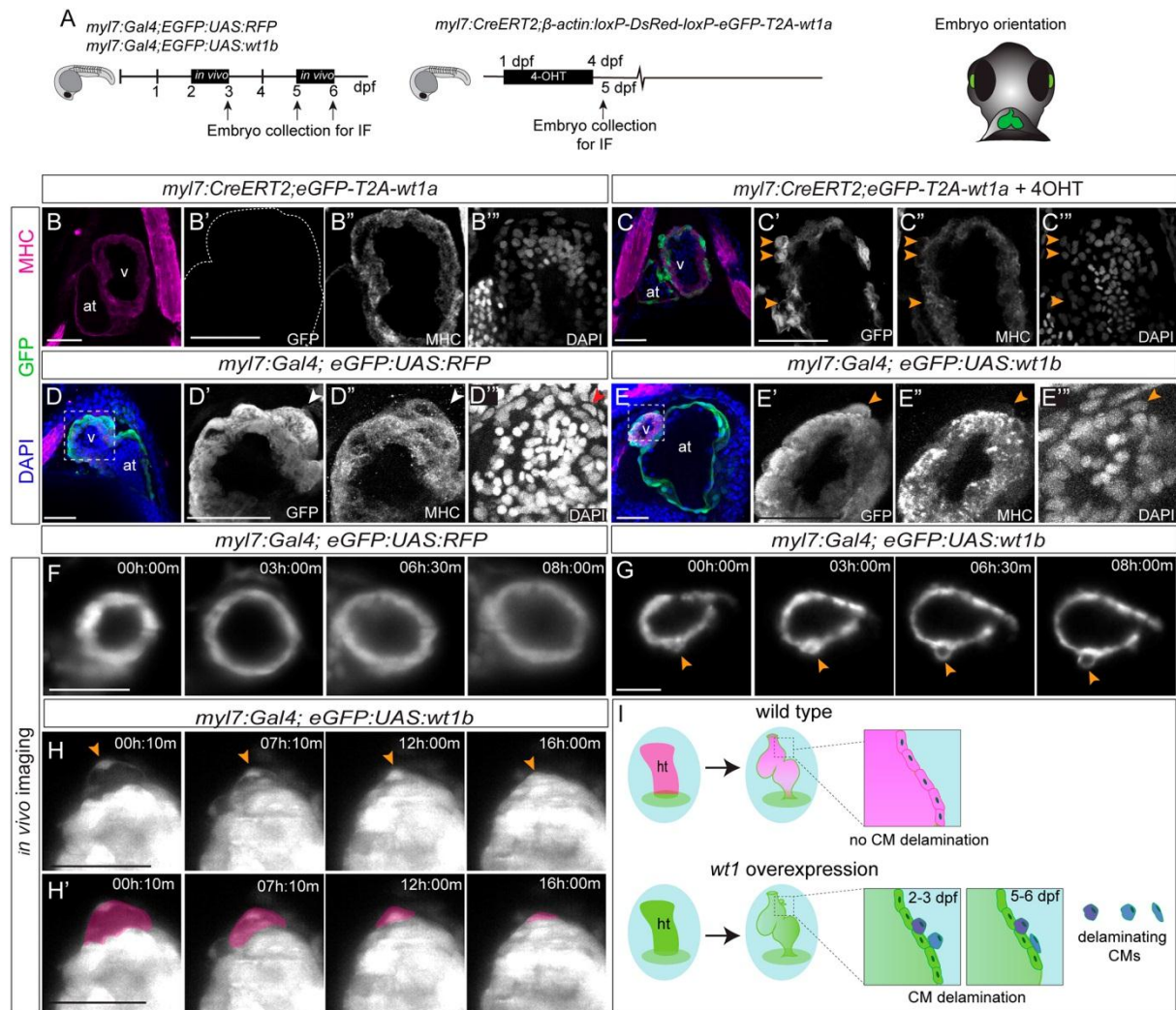


Fig.2. Ventricular cardiomyocytes delaminate from the ventricle and change their fate upon *wt1b* overexpression.

(A) Schematic representation of used transgenic lines and position of the embryos for imaging.

(B-C''') Whole mount immunofluorescence against GFP (green) and MHC (magenta) on *myl7:CreERT2,eGFP-T2A-wt1a* hearts at 5 days post fertilization (dpf), non-recombined (B-B''') and recombined by addition of 4-OHT between 1 and 4 dpf (C-C'''). Shown are maximum intensity projections of 5 optical sections with 1.5 μ m between two consecutive sections. Arrowheads highlight GFP positive cardiomyocytes located on the apical myocardial surface revealing reduced MHC staining.

(D-E''') Whole mount immunofluorescence against GFP and MHC on a *myl7:Gal4;eGFP:UAS:RFP* (D-D''') and a *myl7:Gal4;eGFP:UAS:wt1b* (E-E''') embryo, at 3 dpf. DAPI was used for nuclear counterstain. Shown are maximum intensity

projections of 20 stacks with a distance of 1 μm between two consecutive optical sections of the heart region. (D'-D''') and (E'-E''') are magnifications of the area of the ventricle marked by the dashed bounding boxes in D and E, respectively. Arrowhead points to a GFP-positive cell that is MHC⁺ in D'-D''' and to a GFP+/MHC- cell in E'-E''' and to an epicardial cell in the *myl7:Gal4;eGFP:UAS:RFP* control heart, negative for both GFP and MHC.

(F-G) Time lapse images of the ventricle in a *myl7:Gal4; eGFP:UAS:RFP* (F) or *myl7:Gal4; eGFP:UAS:wt1b* (G) embryo between 2 and 3 dpf. Elapsed time since initial acquisition is stamped in each panel. Arrowhead points to a cell extruding from the ventricle.

(H-H') Time lapse images of the ventricle in a *myl7:Gal4; eGFP:UAS:wt1b* embryo between 5 and 6 dpf. Elapsed time since initial acquisition is stamped in each panel. Note how delaminating cells change morphology along time and flattens down (arrowhead). In H' the flattening cells are highlighted in magenta.

(I) Model of the delamination process of *wt1b* overexpressing cardiomyocytes.

Scale bar, 50 μm . at, atrium; CM, cardiomyocyte; ht, heart tube; IF, immunofluorescence; v, ventricle.

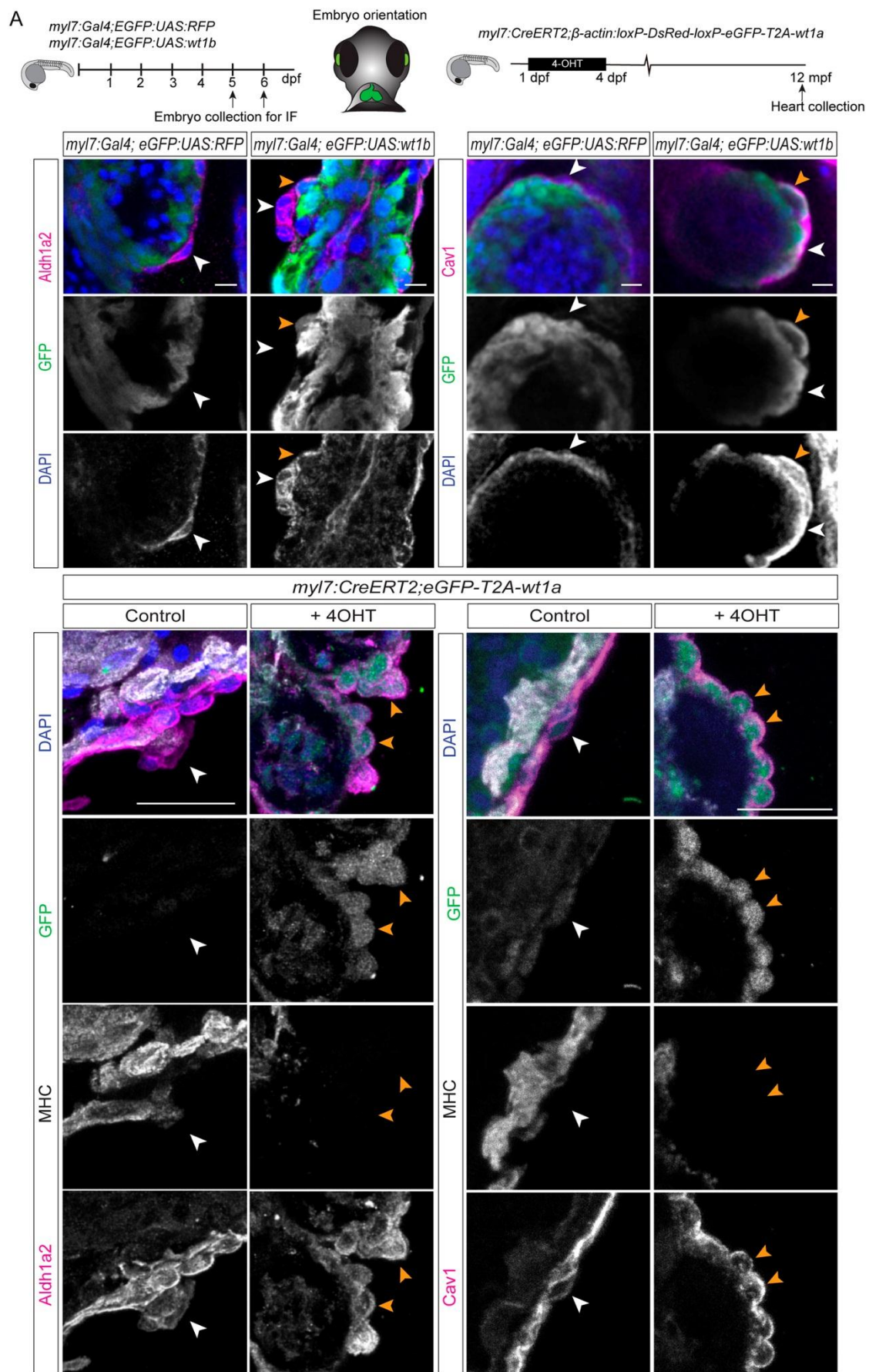


Fig.3. Delaminated *wt1* overexpressing in cardiomyocytes start to express epicardial markers.

(A) Schematic representation of the lines used and the time points during which 4-hydroxytamoxifen (4-OHT) was administered to *myl7:CreERT2;β-actin:loxP-DsRed-loxP-eGFP-T2A-wt1a* fish (in short *myl7:CreERT2,eGFP-T2A-wt1a*), as well as embryo orientation for image acquisition. Shown is also the embryo orientation for image acquisition.

(B-C'') Whole mount immunofluorescence against GFP and Aldh1a2 in *myl7:Gal4;eGFP:UAS:RFP* (B-B'') and *myl7:Gal4;eGFP:UAS:wt1b* (C-C'') embryos, at 5 days post-fertilization (dpf). Shown are maximum intensity projections of 5 images with a distance of 1.5 μm between two consecutive optical sections. White arrowheads mark cells positive for Aldh1a2. Orange arrowheads indicate cells that are positive for both GFP and Aldh1a2. Green, GFP; magenta, Aldh1a2; blue, DAPI.

(D-E'') Whole mount immunofluorescence against GFP and Caveolin 1 (Cav1) in *myl7:Gal4;eGFP:UAS:RFP* (D-D'') and *myl7:Gal4;eGFP:UAS:wt1b* (E-E'') embryos, at 6 dpf. Shown are maximum intensity projections of 10 consecutive optical section with a distance of 1.5 μm between them. White arrowheads highlight epicardial cells positive for Cav1 and negative for GFP. Orange arrowheads indicate epicardial cells that express both Cav1 and GFP. Green, GFP; magenta, Cav1; blue, DAPI.

(F-G''') Immunofluorescence against GFP (green), MHC (white) and Aldh1a2 (magenta) on paraffin sections of *myl7:CreERT2;eGFP-T2A-wt1a* and *myl7:CreERT2;eGFP-T2A-wt1a + 4-OHT* adult hearts. Shown are zoomed views of heart sections in the atrium. Both, merged and single channels are shown, as indicated in the panel. White arrowheads, cells positive for Aldh1a2 only. Orange arrowheads point to cells positive for GFP and Aldh1a2 signal that lack MHC staining, and which are located close to the myocardial surface.

(H-I'') Immunofluorescence against GFP (green), MHC (white) and Caveolin 1 (Cav1) (magenta) on paraffin sections of *myl7:CreERT2;eGFP-T2A-wt1a* and *myl7::CreERT2;eGFP-T2A-wt1a + 4-OHT* adult hearts. Shown are zoomed views of heart sections in the atrium. Both, merged and single channels are shown, as indicated in the panel. White arrowheads point to cells positive only for Cav1. Orange arrowheads point to cells positive for GFP and Cav1 signal that lack MHC staining, and which are located close to the myocardial surface.

Scale bars: 10 μm (B-E'') and 25 μm (F-I'''). Cav1, Caveolin1; MHC, Myosin Heavy Chain.

(F-M') Immunofluorescence against tdTomato (tdT) (using a DsRed antibody) and MHC in *myl7:cdh2-tdTomato* (F-I') and *myl7:cdh2-tdTomato;myl7:Gal4;eGFP:UAS:wt1b* (J-M') embryos. (F-G) 3D projections of a heart. (G) Zoomed view of the box region in F'. (H-I') Sagittal single planes of the ventricle. (I-I') Zoomed view of the box in H'. Arrowheads point to regions with tdT signal. (J-K'') 3D projections of a heart. (J'') Zoomed view of the box in J'. (K-K'') Zoomed views of the box in J. Arrowheads point to delaminating cells from the ventricle. Note the absent tdT signal from the delaminated cells (K''). (L-M') Sagittal single planes of the ventricle. (M-M') Zoomed view of the box in I. Arrowheads highlight tdT signal.

(N-Q') Immunofluorescence against β -catenin (β -cat) and MHC in *myl7:Gal4;eGFP:UAS:RFP* (N-O') and *myl7:Gal4;eGFP:UAS:wt1b* (P-Q') embryos. Shown are sagittal single planes of the ventricle of merged and single channels as marked in the panels. LUT color shows gradient of β -cat signal intensity. (O-O') and (Q-Q') are zoomed views of the box in N and P, respectively. Marked region in P' indicates the ventricle.

(R-U') Immunofluorescence against Laminin (Lam) and MHC in *myl7:Gal4;eGFP:UAS:RFP* (R-S') and *myl7:Gal4;eGFP:UAS:wt1b* (T-U') embryos. Shown are sagittal single planes of the ventricle of merged and single channels as marked in the panels. LUT color shows gradient of laminin signal intensity. (S-S') and (U-U') are zoomed views of the box in R' and T, respectively. Arrowheads highlight Laminin signal.

Scale bar: 50 μ m (B-B', D-D', F-F', H-H', J-J', L-L', N-N', P-P', R-R' and T-T'); 10 μ m (C-C', E-E', G, I-I', K-K'', M-M', O-O', Q-Q', S-S' and U-U').

dpf; days post fertilization; IF, immunofluorescence.

(B-F') Immunofluorescence against GFP and myosin heavy chain (MHC) on *myl7:Gal4; eGFP:UAS:RFP* and *myl7:Gal4;eGFP:UAS:wt1b* zebrafish embryos. (B-C') 3D projection of 1 day post fertilization (dpf) embryos. Shown are lateral views of the cardiac tube. Asterisk in C' indicates the heart, where MHC is absent. (D) MHC staining of the myotome region of the *myl7:Gal4; eGFP:UAS:wt1b* embryo. (E-F') 3D projections of the heart region at 6 dpf. Shown are ventral views, the head is to the top.

(G) Quantification of mean fluorescence intensity in the heart region for *myl7:Gal4; eGFP:UAS:RFP* and *myl7:Gal4;eGFP:UAS:wt1b* zebrafish, at indicated developmental stages. Statistical significance was calculated by unpaired t-test, with Welch's correction (24 hpf) and unpaired t-test for the remaining group comparisons. Means \pm SD as well as individual measurements, representing biological replicates, are shown.

(H-I) Whole mount mRNA *in situ* hybridization against *myl7* mRNA in (H) *eGFP:UAS:wt1b* and (I) *myl7:Gal4;eGFP:UAS:wt1b* zebrafish embryos at 3 dpf. Embryos are positioned ventrally, with the head to the top.

(J-K') Immunofluorescence against GFP and Alcam on *myl7:Gal4;eGFP:UAS:RFP* and *myl7:Gal4;eGFP:UAS:wt1b* zebrafish embryos. Shown are 3D projection of the heart region in a 6 dpf old larva (ventral views, the head is to the top).

(L) Quantification of mean fluorescence intensity of anti-Alcam staining as shown in J-K'. Statistical significance was calculated by unpaired t-test, with Welch's correction. Shown are mean \pm SD as well as individual measurements, representing biological replicates.

(M-P') Immunofluorescence against GFP and α -Actinin. Shown are maximum intensity projections of two consecutive optical sections with a step size of 1.5 μ m of the ventricle of *myl7:Gal4;eGFP:UAS:RFP* (M-N) and *myl7:Gal4;eGFP:UAS:wt1b* (O-P') at 6 dpf. (N,N' and P,P') Maximum intensity projections of boxed regions in (M) and (O), respectively.

(Q-R') Serial block face scanning electron microscope images of zebrafish hearts. Shown are single sections of *myl7:Gal4;eGFP:UAS:RFP* (Q-Q') and *myl7:Gal4;eGFP:UAS:wt1b* (R,R') hearts. Different cell layers are highlighted with colors. (Q' and R') Zoomed areas of Q and R highlighting sarcomeres. Green labels the epicardium, magenta marks the endocardial layer and orange highlights the

myocardium. Orange arrowheads, z-bands; Cyan arrowhead, basement membrane delimiting epicardium and myocardium.

Scale bars, 50 μm (B-F', H-M and O,O'); 1 μm (Q and R), 500 nm (Q' and R'), 10 μm (N,N' and P,P'). at, atrium; BM, basement membrane; CM, cardiomyocyte; ECM, extracellular matrix; EnC, endothelial cell; EpC, epicardial cell; Ery, erythrocyte; v, ventricle; z, z-line. Green, GFP; magenta, MHC, Alcam; blue, DAPI.

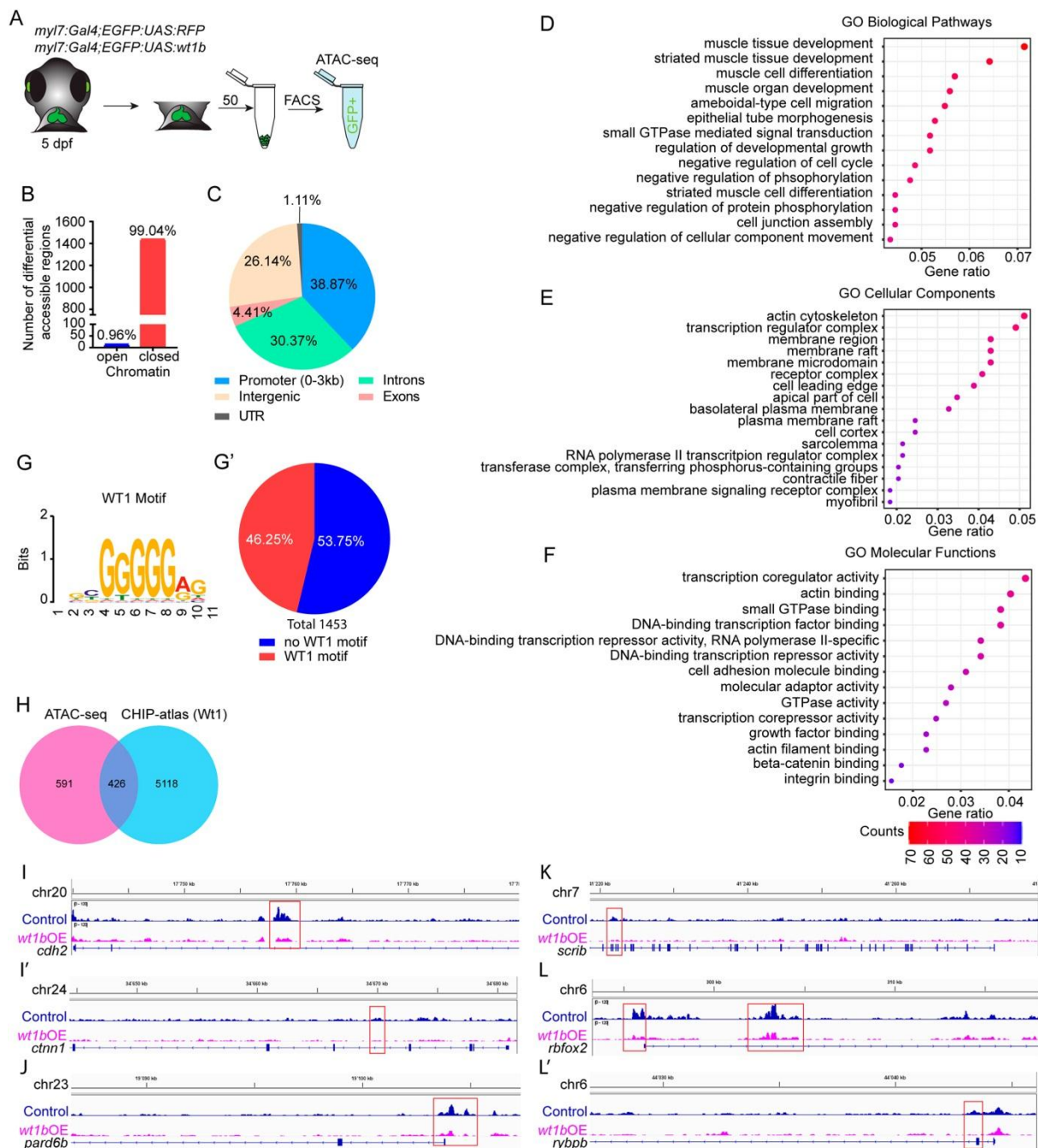


Fig.6. Assay for Transposase-Accessible Chromatin sequencing (ATAC-seq) in *wt1b*-overexpressing cardiomyocytes.

(A) Schematic representation of cell acquisition for ATAC-seq.

(B) Graphical representation of number of differential accessible regions between *myl7:Gal4; eGFP:UAS:RFP* and *myl7:Gal4; eGFP:UAS:wt1b* cardiomyocytes at 5 days post-fertilization (dpf).

(C) Distribution of the genomic regions with differential accessible regions.

(D-F) Gene Ontology (GO) pathways enrichment for differential accessible regions in cardiomyocytes after *wt1b*-overexpression. (D) Shown are selected GO Biological

Pathways enrichment out of the top 25. (E) Shown are selected GO Cellular Components enrichment out of the top 25. (F) Shown are selected GO Molecular Functions enrichment out of the top 25. The color scale indicates the number of genes enriched in a pathway. All pathways have enrichments significance $p\text{-adjust} \leq 0.05$.

(G-G') MEME-Centrimo WT1 motif analysis. (G') Percentage of the differential accessible regions in which the WT1 motif is represented.

(H) Venn Diagram comparing the number of differential accessible regions that are common between the ATAC-seq and the CHIP-atlas database for WT1.

(I-L') Sequencing tracks for genes with differential peaks within their genomic loci. Shown are genes representative of adherens junctions: *cdh2* (I) and *ctnn1* (I'); apical polarity, *pard6b* (J); basal polarity, *scrib* (K); and sarcomere assembly: *rbfox2* (L) and *rybpb* (L').

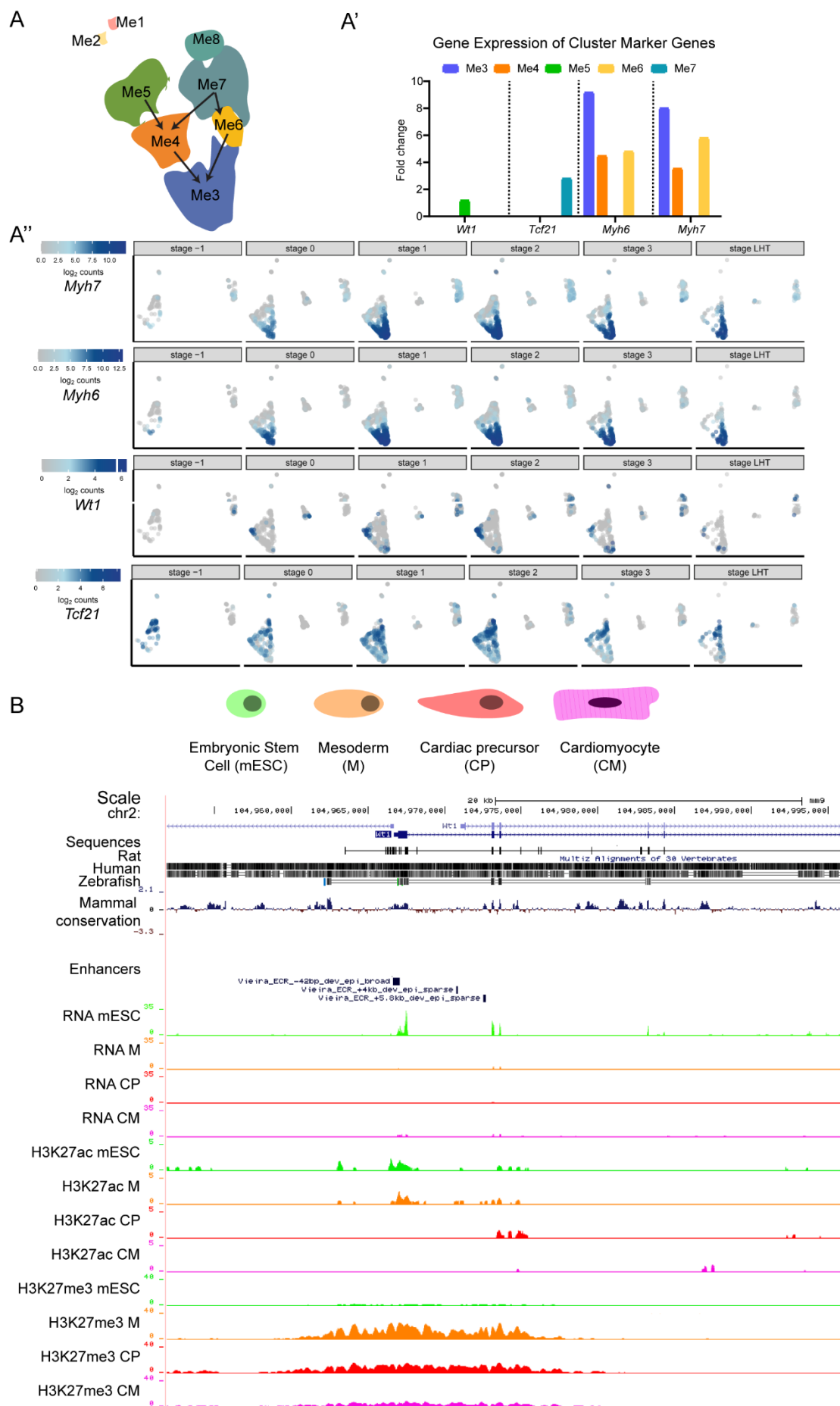


Fig. S1.

Fig. S1. Transcriptional and histone modification signatures of *Wt1* through cardiac developmental and differentiation stages *in vivo* and *in vitro* across mouse heart and embryonic stem cells.

(A-A'') Re-analysis of published single cell RNAseq data from mouse embryos (Tyser et al., 2021). (A) Schematic representation of the developmental trajectories of mesothelial cardiac cell populations (Tyser et al., 2021). (A') Fold change in the expression levels of cluster marker genes: *Wt1*, *Tcf21*, *Mhy6* and *Myh7*. (A'') Spatio-temporal gene expression of genes shown in A' in different developmental cardiac cell trajectories. (B) UCSC browser gene tracks depicting the *Wt1* locus and associated transcriptomic and epigenomic signatures in mouse embryonic stem cells (mESC), mesodermal progenitors (M), cardiac precursors (CP) and cardiomyocytes (CM), as published previously (Wamstad et al., 2012). Tracks of activating H3K27ac and repressive H3K27me3 marks are shown and co-localizing elements with previously validated epicardial enhancer activities 4kb and 5.8kb downstream of the *Wt1* transcriptional start site (TSS) are indicated (Vieira et al., 2017). Shown tracks represent the sum of the tracks for the different samples, for each type of cell. Mammal conservation is illustrated by the Placental Mammal base wise conservation track by PhyloP.

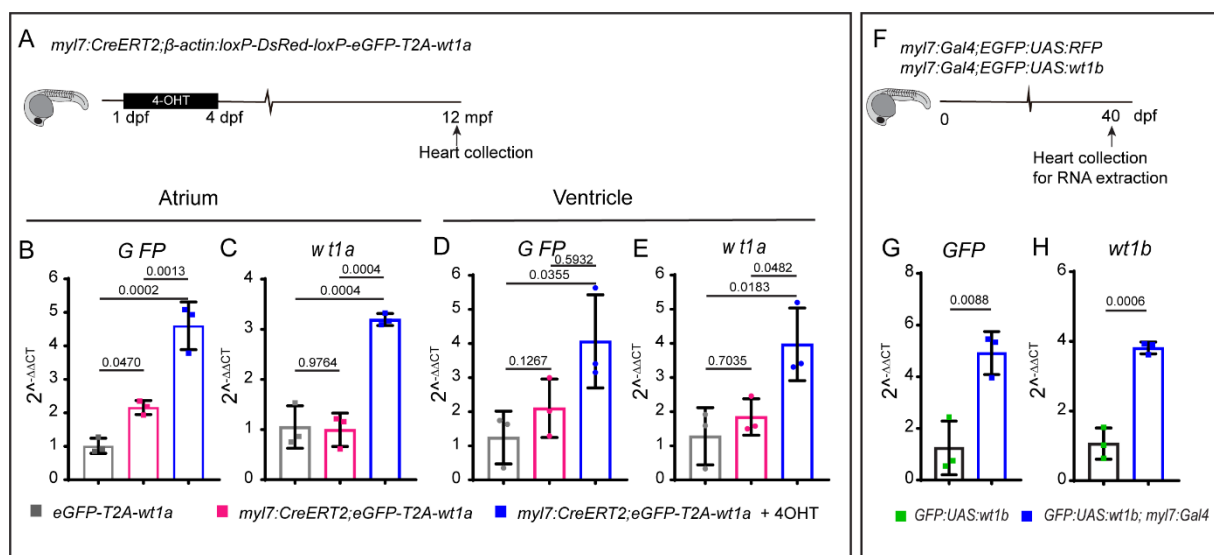


Fig. S2

Fig. S2. Validation of the *wt1a* and *wt1b* overexpression lines.

(A) Schematic representation of the time points during which 4-Hydroxytamoxifen (4-OHT) was administered to *myl7:CreERT2;β-actin:loxP-DsRed-loxP-eGFP-T2A-wt1a* fish (in short *myl7:CreERT2,eGFP-T2A-wt1a*) and tissue collection.

(B-E) qRT-PCR for *GFP* (B,D) and *wt1a* (C,E) on adult heart cDNA from *myl7:CreERT2, eGFP-T2A-wt1a* with and without 4-OHT. qRT-PCR was performed on cDNA obtained from the atrium (B,C) and (D,E) ventricles. Points represent biological replicates, 3 for each group. Statistical significance was calculated using one-way ANOVA. Shown are means \pm SD.

(F) Schematic representation of lines used and the time at which RNA was extracted.

(G-H) qRT-PCR for *eGFP* (G) and *wt1b* (H) in *eGFP:UAS:wt1b* and *myl7:Gal4;eGFP:UAS:wt1b* hearts at 40 days post fertilization (dpf). The points represent biological replicates. Statistical significance was calculated with an unpaired t-test. Shown are also means \pm SD.

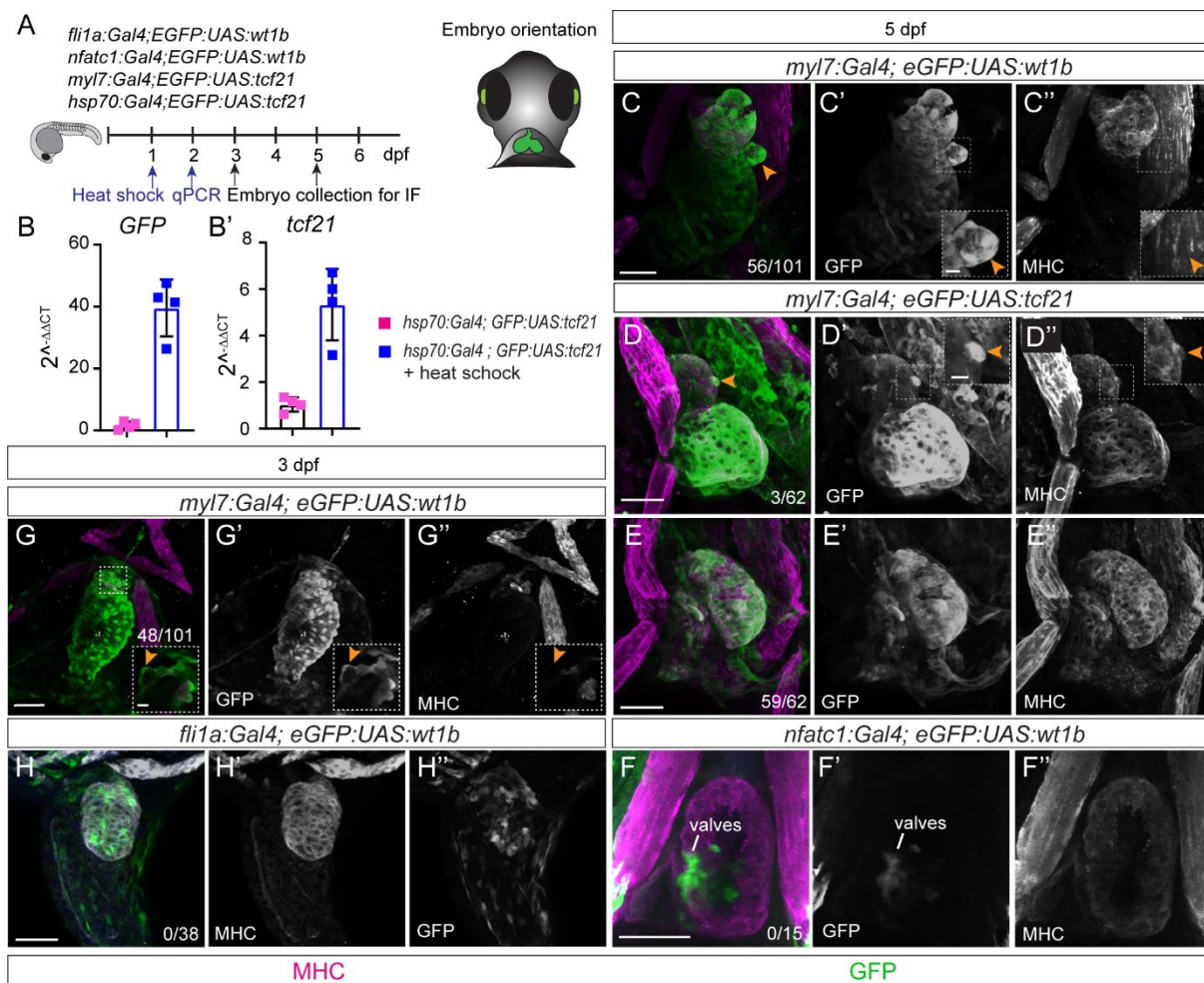


Fig. S3

Fig. S3. Overexpression of *tcf21* transcription factor in cardiomyocytes and *wt1b* in non-cardiomyocytes does not affect heart development.

(A) Schematic representation of the lines used and embryo orientation for imaging. (B-B') qRT-PCR for GFP (B) and *tcf21* (B') on 48 hours post-fertilization (hpf) zebrafish embryos. cDNA from *hsp70:Gal4;eGFP:UAS:tcf21* with and without heat-shock. Points represent biological replicates, 3 for each group. Statistical significance was calculated using unpaired t-test with Welch's correction. Shown are means \pm SD. (C-H'') Immunofluorescence against GFP and myosin heavy chain (MHC) on *myl7:Gal4;eGFP:UAS:wt1b*, *myl7:Gal4;eGFP:UAS:tcf21*, *fli1a:Gal4;eGFP:UAS:wt1b* and *nfatc1:Gal4;eGFP:UAS:wt1b* zebrafish embryos, at 3 or 5 days post fertilization (dpf). (C-C'') Shown are 3D projections of a *myl7:Gal4;eGFP:UAS:wt1b* heart in a ventral view, at 5 dpf. (C'-C'') show single channels for GFP and MHC. The box highlights a zoomed region in the heart where a cluster of delaminating cells can be seen. (C'') Note the absence of MHC in the delaminated cells. (D-E'') Shown are 3D

projections of a *myl7:Gal4;eGFP:UAS:tcf21* heart in a ventral view, at 5 dpf. (D-D'') show single channels for GFP and MHC. The box highlights a zoomed region in the heart with one cell delaminating. Note in D'' that the delaminating cell preserved MHC expression. (F-F'') Shown are maximum intensity projections of 5 stacks with a distance of 1.5 μm between two consecutive optical sections of the heart region of a *nfatc1:Gal4;eGFP:UAS:wt1b* heart in a ventral view, at 5 dpf. GFP expression is observed in the valve region. The number of embryos with delaminating cells is indicated in the panels. Green, GFP; magenta, MHC. Scale bar 50 μm and 10 μm , in the zoom boxes. at, atrium; v, ventricle.

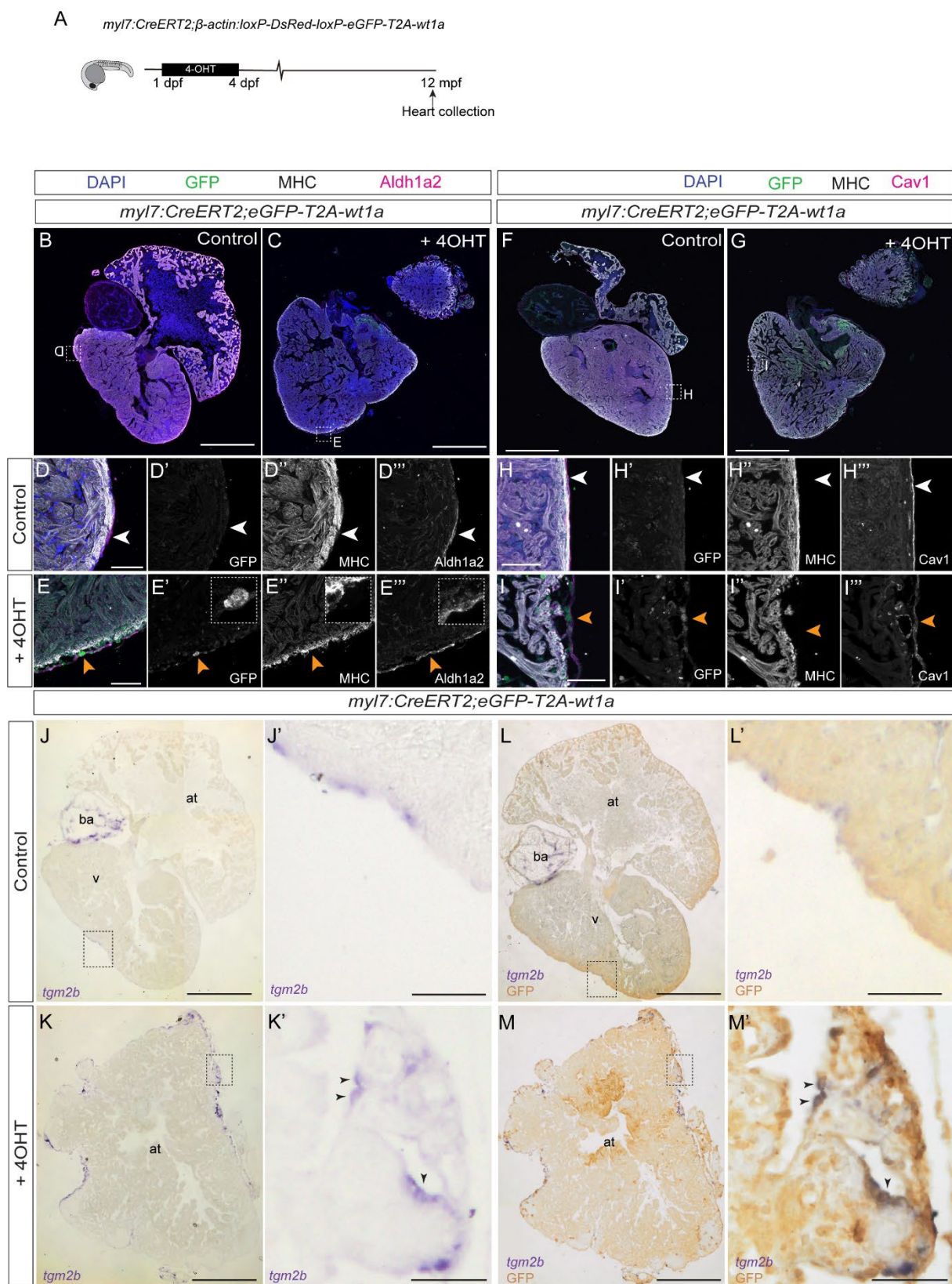


Fig. S4

Fig. S4. *wt1a* overexpression in cardiomyocytes induces expression of epicardial markers in the adult heart.

(A) Schematic representation of the time points during which 4-hydroxytamoxifen (4-OHT) was administered to *myl7:CreERT2;β-actin:loxP-DsRed-loxP-eeGFP-T2A-wt1a* fish (in short *myl7:CreERT2,eeGFP-T2A-wt1a*) and tissue collection.

(B-E'') Immunofluorescence against GFP (green), MHC (white) and Aldh1a2 (magenta) on paraffin sections of *myl7:CreERT2;eGFP-T2A-wt1a* and *myl7:CreERT2;eGFP-T2A-wt1a* + 4-OHT adult hearts. Shown are whole heart sections (B,C) and zoomed views in the ventricle (D-E''). Zoomed views have been rotated to facilitate comparison between control and overexpression panels. Merged and single channels are shown, as indicated in the panel. White arrowheads, cells positive for Aldh1a2 only. Orange arrowheads point to cells positive for GFP and Aldh1a2 signal that lack MHC staining, and which are located close to the myocardial surface.

(F-I'') Immunofluorescence against GFP (green), MHC (white) and Caveolin 1 (Cav1) (magenta) on paraffin sections of *myl7:CreERT2;eGFP-T2A-wt1a* and *myl7:CreERT2;eGFP-T2A-wt1a* + 4-OHT adult hearts. Shown are whole heart sections (F,G) and zoomed views in the ventricle (H,I''). Merged and single channels are shown, as indicated in the panel. White arrowheads point to cells positive only for Cav1. Orange arrowheads point to cells positive for GFP and Cav1 signal that lack MHC staining, and which are located close to the myocardial surface.

(J-M') *in situ* mRNA hybridization against *tgm2b* and immunohistochemistry against eGFP on paraffin sections of *myl7:CreERT2,eeGFP-T2A-wt1a* (J,J' and L,L') and *myl7:CreERT2,eeGFP-T2A-wt1a* + 4-OHT (K,K' and M,M') adult hearts. (J-K') images of sections after *in situ* mRNA hybridization against the epicardial marker *tgm2b*. (L-M'), same section as in J-K' after eGFP immunohistochemistry. Black arrowheads in K' and M' indicate double positive cells for *tgm2b* and eGFP.

Scale bars: 2000 μm (B, C, F, G, J and L), 50 μm (J', K', L' and M') and 10 μm (D-E'' and H-I''). at, atrium; ba, bulbus arteriosus; Cav1, Caveolin1; MHC, Myosin Heavy Chain; v, ventricle.

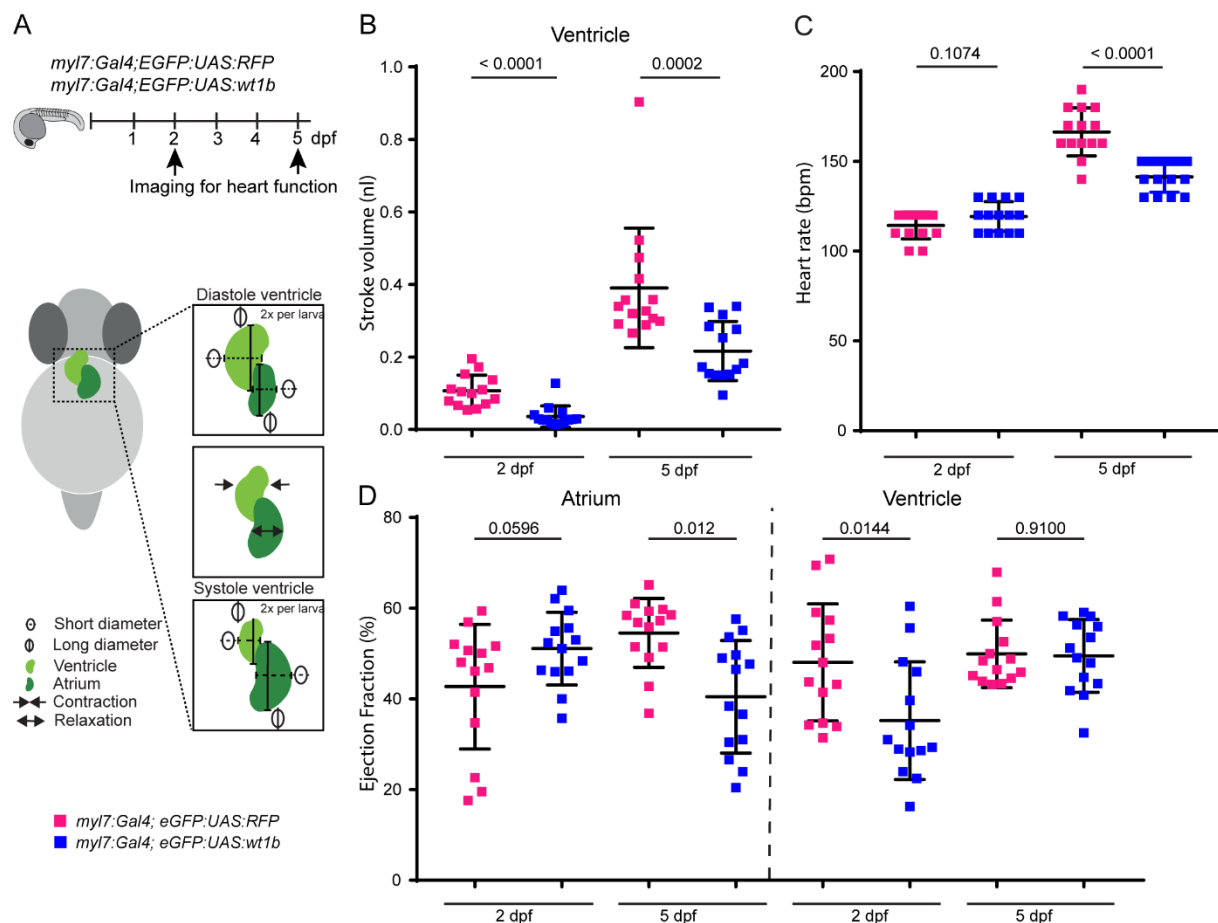


Fig. S5

Fig. S5. Heart function is impaired upon overexpression of *wt1b* in cardiomyocytes.

(A) Schematic representation of the lines used and embryo positioning for image acquisition and the parameters used to determine cardiac function in *myl7:Gal4;eGFP:UAS:RFP* and *myl7:Gal4; eGFP:UAS:wt1b*.

(B) Quantification of ventricular stroke volume at 2 days post fertilization (dpf) and 5 dpf. Statistical significance was calculated with the Mann-Whitney test.

(C) Quantification of the heart rate at 2 dpf and 5 dpf. Statistical significance calculated with an unpaired t-test.

(D) Quantification of ventricular ejection fraction at 2 dpf and 5 dpf. Statistical significance was calculated with an unpaired t-test for the comparison between groups in the atrium and in the ventricle at 2 dpf. Mann-Whitney test was applied to calculate the statistical significance between the groups in the ventricle, at 5 dpf.

In all graphs each point represents one embryo. Shown are also means \pm SD.

GO pathways of differential accessible regions for WT1 motif enriched peaks

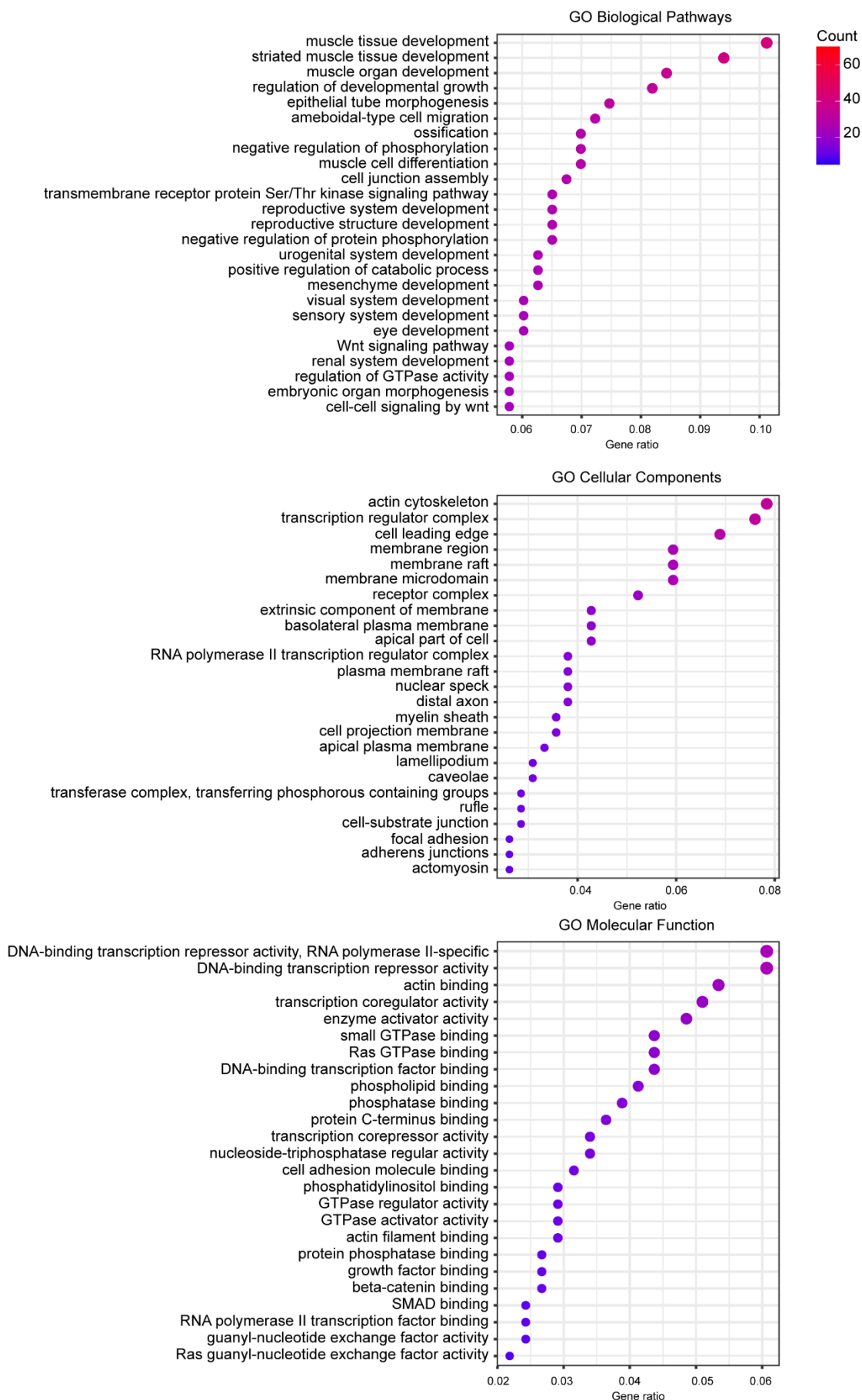
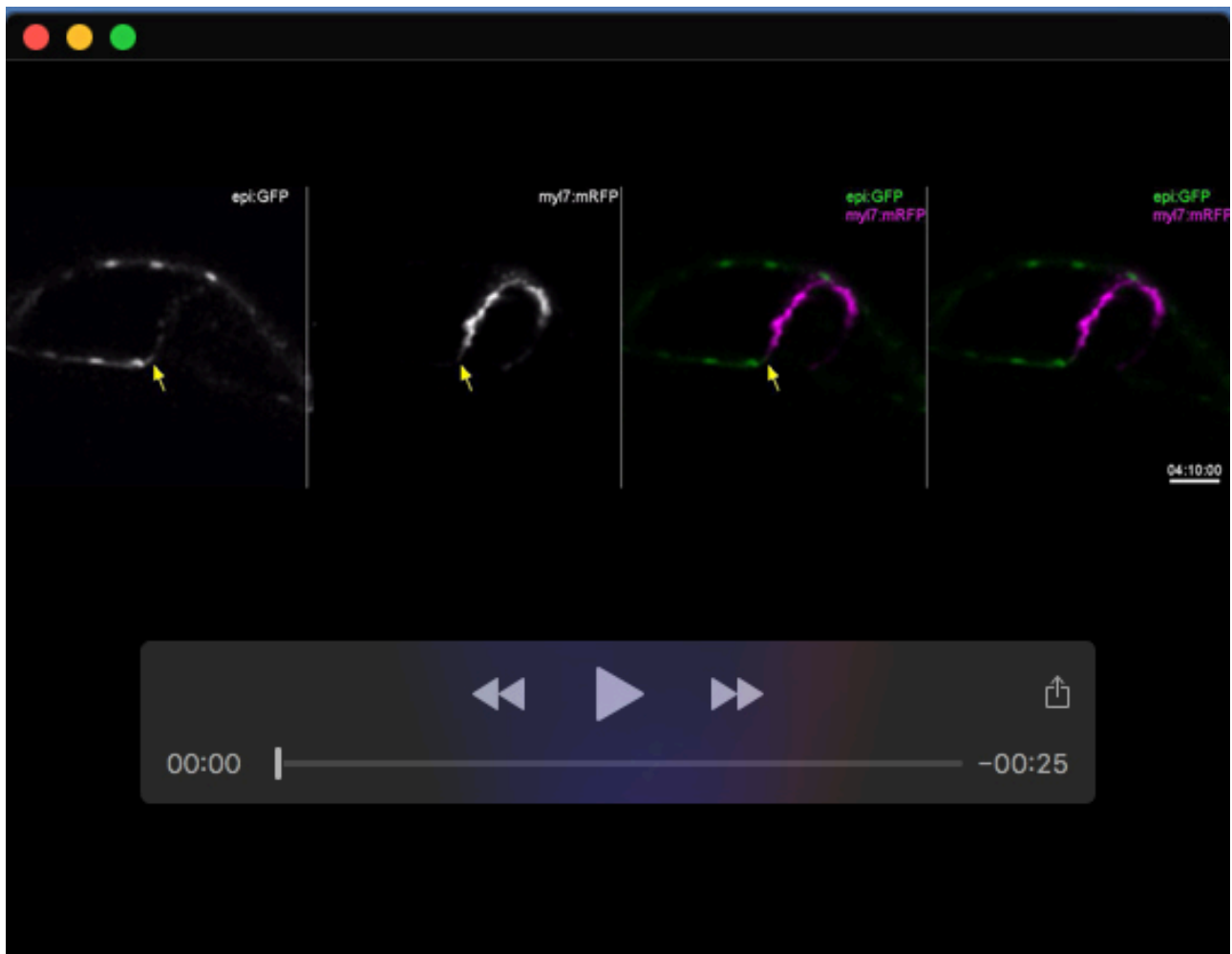


Fig. S6

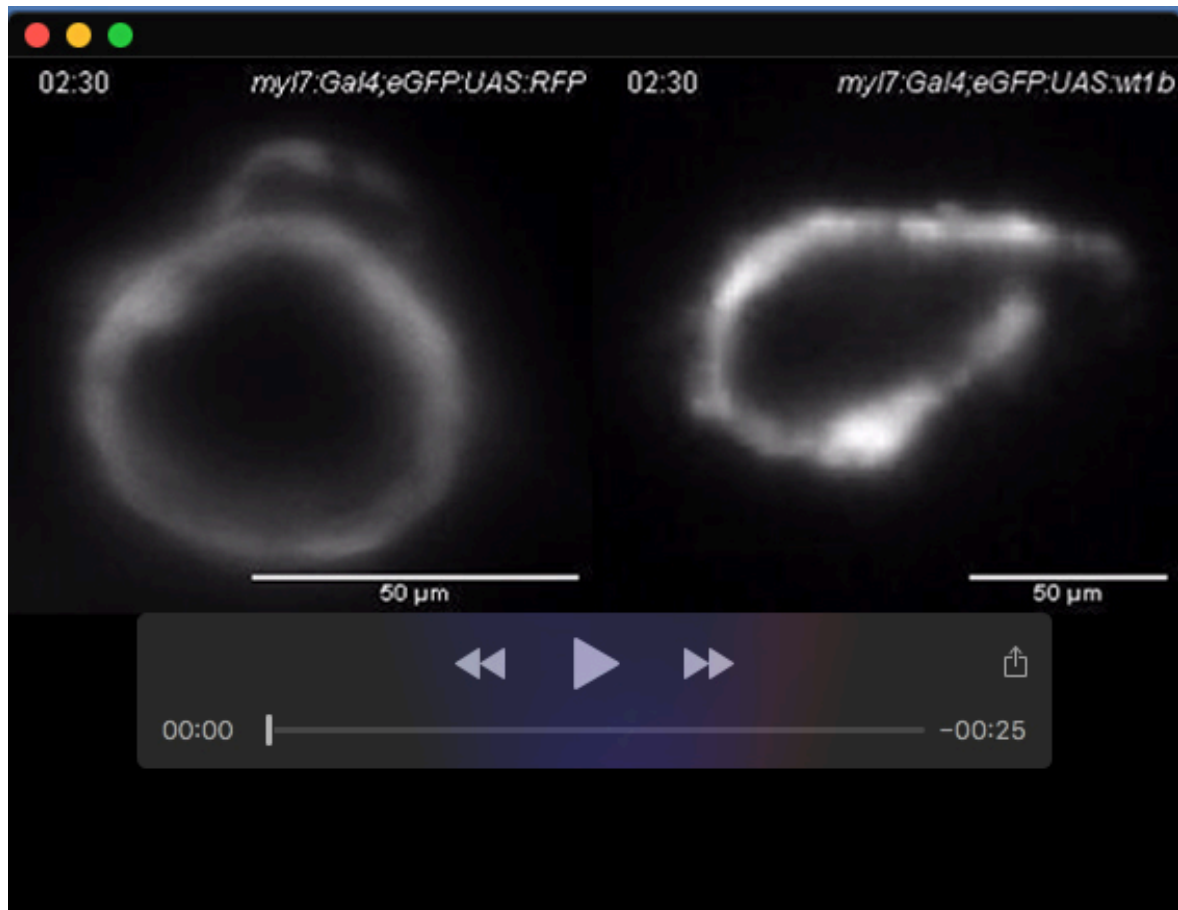
Fig. S6. Gene Ontology pathways of differential accessible regions for WT1 motif enriched peaks.

Gene Ontology (GO) pathways enrichment for differential accessible regions that contain the WT1 motif. Shown are the top 25 Biological, Cellular Components and the Molecular Function pathways.



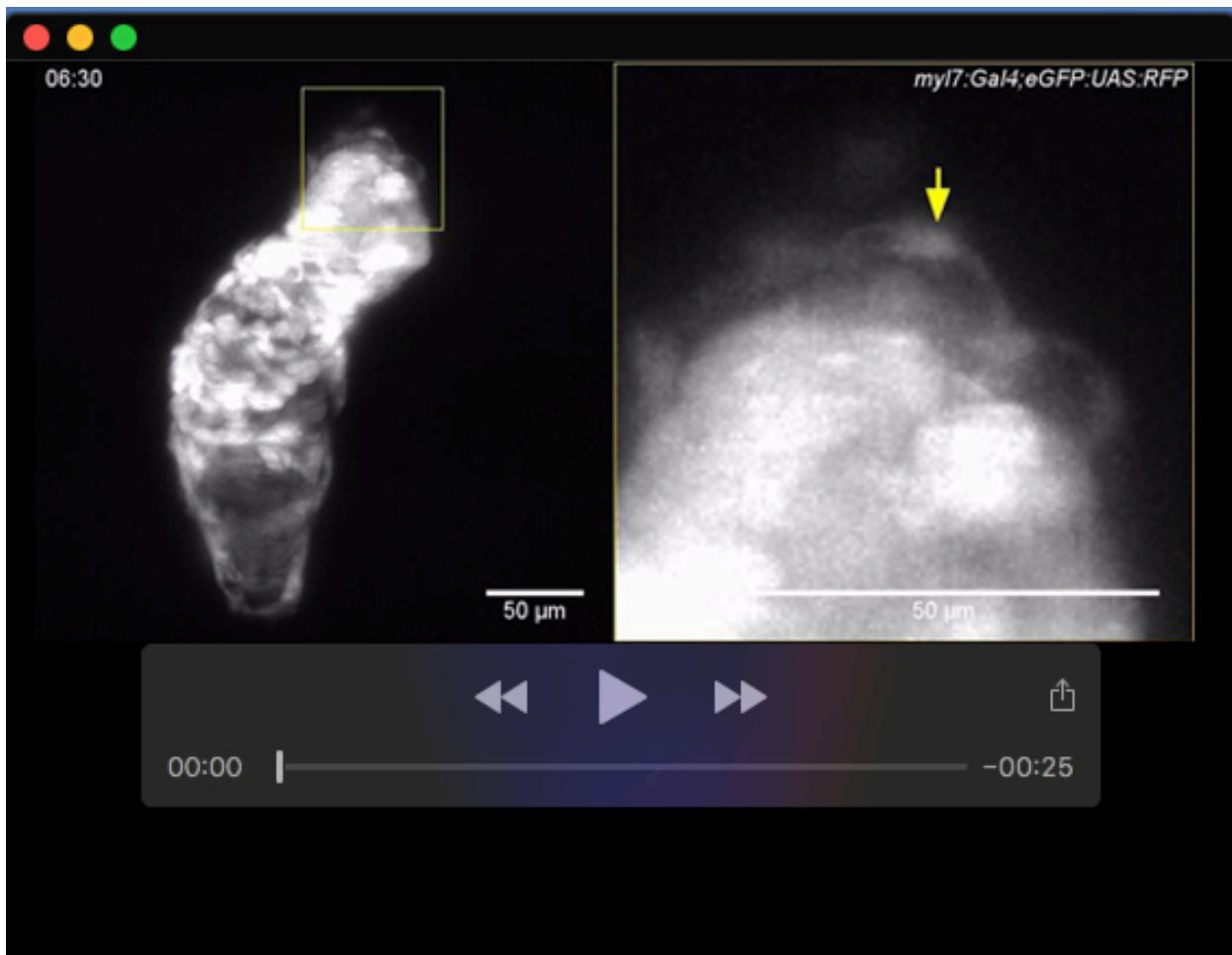
Movie 1. *epi:eGFP*-positive cells at the venous pole switch off GFP expression and start expressing *myl7:mRFP* when entering the heart tube.

In vivo time-lapse imaging of a *epi:GFP;myl7:mRFP* heart between 52 hpf and 68 hpf. The yellow arrow highlights a cell that initially is only GFP positive and latter stops expressing GFP and starts to express RFP. The cyan arrows point to cardiomyocytes in the heart tube that are still GFP-positive at the beginning of the Movie and then loose GFP signal concomitant with increase in mRFP signal intensity. Images were acquired with the Leica TCS SP8 DLS. Shown is a single plane reconstruction of the beating. Scale bar, 50 μ m.



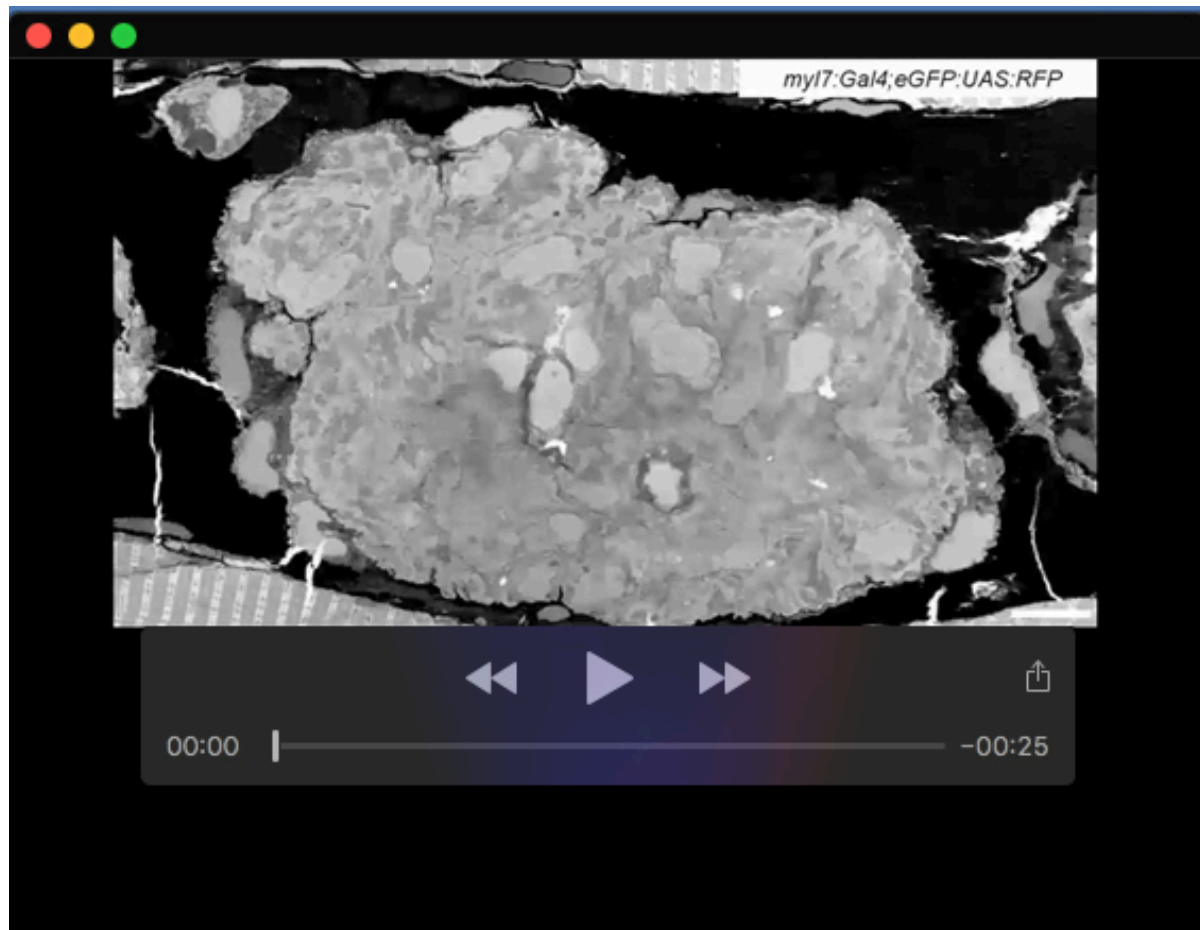
Movie 2. Apical delamination of a *wt1b*-overexpressing cardiomyocyte in a cardiac ventricle at 2 dpf.

In vivo time-lapse imaging of a *myl7:Gal4;eGFP:UAS:RFP* and a *myl7:Gal4;eGFP:UAS:wt1b* heart between 2 and 3 days post fertilization (dpf) acquired with the Leica TCS SP8 DLS confocal microscope, using the digital light sheet (DLS) mode. Shown is the reconstruction of a single plane of the beating ventricle. Note the rounded cells extruding from the ventricle in the *myl7:Gal4;eGFP:UAS:wt1b* heart (right panel, arrow). Scale bar, 50 µm.



Movie 3. Apical delamination of a *wt1b*-overexpressing cardiomyocyte in a cardiac ventricle at 5 dpf.

In vivo time-lapse imaging of a *myl7:Gal4;eGFP:UAS:wt1b* heart between 5 and 6 days post fertilization (dpf) acquired with the Leica TCS SP8 DLS confocal microscope, using the digital light sheet (DLS) mode. Shown is the reconstruction of a single plane of the beating ventricle. Note how the extruded cells flatten down during the time course of the Movie (Yellow arrow). Scale bar, 50 µm.



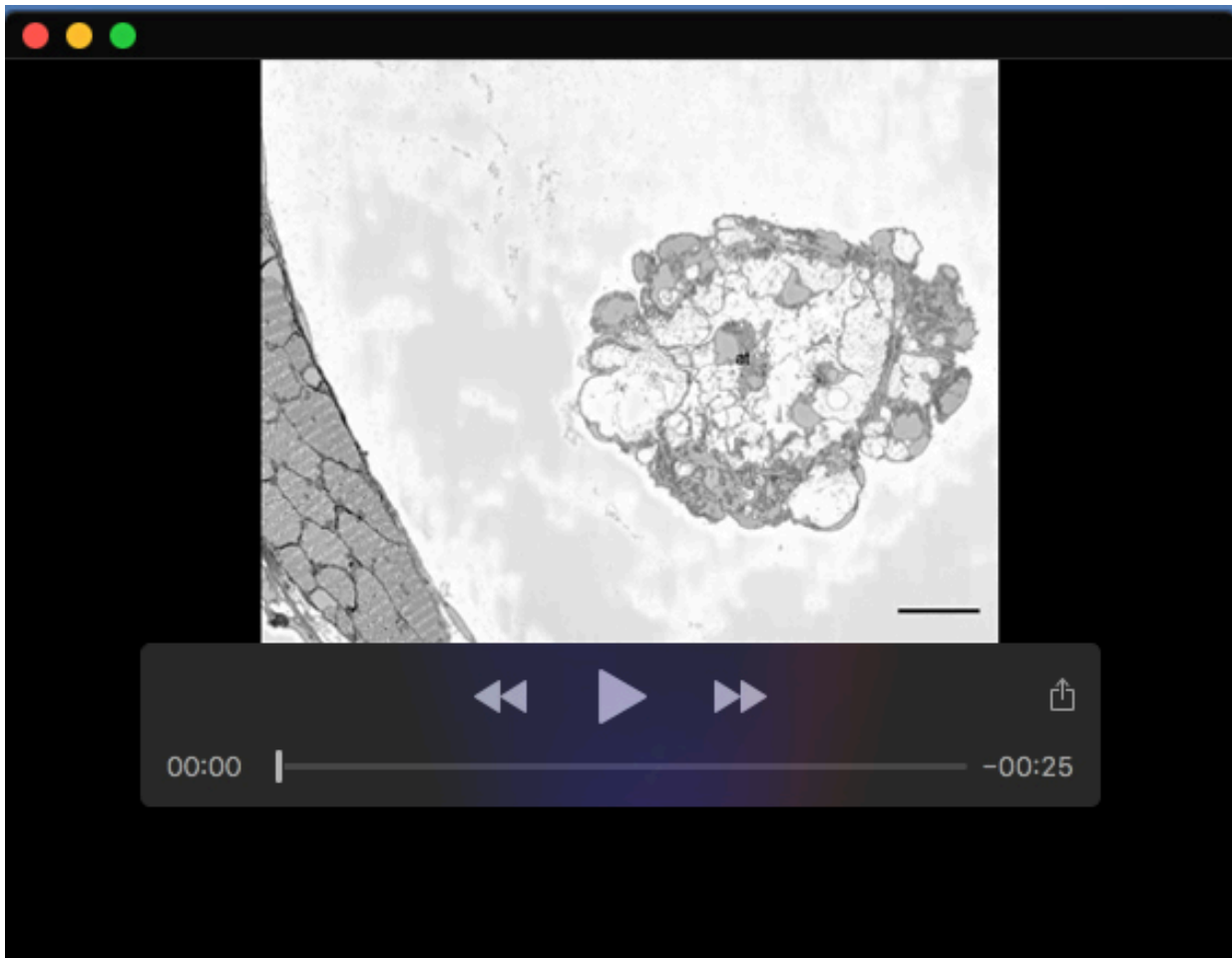
Movie 4. Serial block face scanning z-stacks through a control zebrafish heart at 5 dpf.

Serial stacks through a ventricle from a *myl7:Gal4;eGFP:UAS:RFP* control embryo at 5 dpf. Images were obtained by serial block face scanning electron microscopy. Note the compact organization of the myocardium and the close connection between the myocardium and the endocardium, and how the sarcomeres form a continuous structure between adjacent cardiomyocytes. Of remark is also the dense border between the myocardium and epicardium. EpC, epicardial cell, EnC, endothelial cell, Ery, erythrocyte, CM, cardiomyocyte nuclei. Scale bar 10 μ m.



Movie 5. Zoomed view of a serial block face scanning z-stacks through a control zebrafish heart at 5 dpf.

Serial stacks through a ventricle from a *myl7:Gal4;eGFP:UAS:RFP* control embryo at 5 dpf. Images were obtained by serial block face scanning electron microscopy. Shown is a magnification of the myocardium in a region where sarcomeres can be observed. Note the clearly marked z-lines and the longitudinal continuity of the sarcomeres between adjacent cardiomyocytes. Scale bar, 500 nm.



Movie 6. Serial block face scanning z-stacks through a *wt1b*-overexpressing heart at 5 dpf.

Serial stacks through a ventricle from a *myl7:Gal4;eGFP:UAS:wt1b* embryo at 5 dpf. Images were obtained by serial block face scanning electron microscopy. Note the absence of a compact and organized myocardial layer and the enlarged cardiac jelly separating the endocardium and the myocardium. Also visible the extensive areas filled with extracellular matrix. EpC, epicardial cell, EnC, endothelial cell, Ery, erythrocyte, CM, cardiomyocyte, ECM, extracellular matrix, v, ventricle, at, atrium. Scale bar, 20 μ m.



Movie 7. Zoomed view of a serial block face scanning z-stacks through a *wt1b*-overexpressing heart at 5 dpf.

Serial stacks through a ventricle from a *myl7:Gal4;eGFP:UAS:wt1b* embryo at 5 dpf. Images were obtained by serial block face scanning electron microscopy. Shown here is a magnification of the myocardium in a region where sarcomeres can be observed. Note the z-lines. Remarkable is the disorganized arrangement of the sarcomeres between adjacent cardiomyocytes. Scale bar, 500 nm.

Table S1. Differential Peak Calling.

Sheet 1: The file contains about genomic location and information on fold change and significance values of the differential peaks. Columns J-O indicate in which samples peaks were identified (+) or not (-).

Sheet 2: The file contains the same information as sheet 1, with extra information on Peak class, Gene location and direction, zebrafish gene symbol associated with the peak, gene description, mouse ID and whether the gene can also be found on CHIP atlas database for WT1.

[Click here to download Table S1](#)

Table S2. Gene Ontology.

Full list of pathways and genes enriched in each of them.

[Click here to download Table S2](#)

Table S3. Annotation of differential peaks.

Differential peaks with their associated genes and genomic region classification.

[Click here to download Table S3](#)

Table S4. Key resources

REAGENT/RESOURCE	SOURCE	IDENTIFIER
Antibodies		
Rabbit polyclonal anti-Aldh1a2	GeneTex	Cat# GTX124302
Mouse monoclonal anti-CD166 antigen homologue A (neurolin) (Alcama)	DSHB	Cat # ZN-8
Mouse monoclonal anti α -Actinin (sarcomeric) clone EA-53	Sigma Aldrich	Cat # A7811
Mouse monoclonal anti-Caveolin 1	BD biosciences	Cat# 610406
Chicken polyclonal anti-GFP	Aves Labs	Cat# GFP-1010
Mouse monoclonal anti-myosin, sarcomere (MHC)	DSHB	Cat# MF 20, RRID:AB_2147781
Mouse monoclonal anti-ZO-1 (ZO1-1A12)	Invitrogen	Cat # 33-9100
Rabbit anti-Laminin	Sigma Aldrich	Cat # L9393
Mouse monoclonal anti β -Catenin	BD Biosciences	Cat # 610153
Goat anti-Chicken IgY (H+L), Alexa Fluor [®] 488 conjugate	Thermo Fisher Scientific	Cat # A-11039
Goat anti-Mouse IgG2b, Alexa Fluor [®] 568 conjugate	Thermo Fisher Scientific	Cat # A-21144
Goat anti-Mouse IgG2b, Alexa Fluor [®] 647 conjugate	Thermo Fisher Scientific	Cat #A-21242
Goat Anti-Mouse	Dako	Cat # P 0447
Immunoglobulins/HRP		
Goat anti-Rabbit IgG (H+L) Secondary Antibody, Alexa Fluor [®] 568 conjugate	Thermo Fisher Scientific	Cat # A-11036
Goat anti-Mouse IgG1, Alexa Fluor [®] 568 conjugate	Thermo Fisher Scientific	Cat # A-21124
Primers		
Gene	Forward primer	Reverse Primer
<i>Gfp</i>	CAAGATCCGCCACAACATCG	GACTGGGTGCTCAGGTAGTG
<i>wt1a OE</i>	GAGCCATCCCGGAGGTTATG	GGTACTCTCCGCACATCCTG
<i>wt1b OE</i>	CCAGGTCTGACCAGCTGAAG	GTGTCTTCAGGTGGTCCGAG
<i>tcf21</i>	ATGTCCACCGGGTCCATCAG	TCAGGAAGCTGTAGTCCCGCA
Chemicals, Peptides, and Recombinant Proteins		
4-hydroxytamoxifen	Sigma Aldrich	Cat#H6278
N-Phenylthiourea (PTU)	Sigma Aldrich	Cat# P7629
Proteinase K	Roche	Cat# 03115801001
Heparin sodium salt from porcine intestinal mucosa	Sigma- Aldrich	Cat# H4784
Formamide	Sigma- Aldrich	Cat# 47670-1L-F
Blocking reagent	Sigma-Aldrich	Cat# 11096176001
Ribonucleic acid from torula yeast	Sigma- Aldrich	Cat# R6625-25G
HBSS (10X), no calcium, no magnesium, no phenol red	Thermo Fisher Scientific	Cat# 14185052
Corning™ 0.05%	Thermo Fisher Scientific	Cat# MT25051CI

REAGENT/RESOURCE	SOURCE	IDENTIFIER
Trypsin/0.53 mM EDTA in HBSS w/o Calcium and Magnesium		
Collagenase	Sigma	Cat # C8176
BSA	Sigma	Cat# A3059
Kits		
SMARTer [®] Ultra [™] Low Input RNA for Illumina [®] Sequencing – HV kit	Takara	Cat# 634828
Agilent's High Sensitivity DNA Kit	Agilent	Cat# 5067-4626
Low Input Library Prep Kit	Illumina	Cat# 634947
Illumina Nextera kit	Illumina	Cat# Fc-121-1030
Illumina Tagment DNA TDE1 Enzyme and Buffer Kits	Illumina	Cat# 20034198
DT [®] for Illumina Nextera DNA Unique Dual Indexes Set C	Illumina	Cat# 20027215
Bioline MyFi Mix	Meridian Bioscience	Cat# Bio-25050
MinElute PCR Purification Kit	Qiagen	Cat# 28004
AMPure XP	Beckman Coulter	Cat # A63882
Qubit dsDNA HS Assay Kit	Thermo Fisher Scientific	Cat# Q32854
NGS Fragment Kit	Agilent	Cat# DNf-473
Bioline JetSeq library Quantification Lo-ROX kit	Meridian Bioscience	Cat# Bio-68029
NovaSeq XP 2-Lane Kit v1.5	Illumina	Cat# 20043130
NovaSeq 6000 SP Reagent Kit v1.5	Illumina	Cat# 20040719
Software and Algorithms		
Fiji	NIH	SCR_002285
GraphPad Prism 7	GraphPad Software	SCR_002798
Imaris 9.5.1	Bitplane	
MATLAB R2017a	MathWorks	
Specialized Material		
U-shaped glass capillaries	Leica microsystems	Cat # 158007061
MatTek imaging dish, 35 mm	MatTek Corporation	Cat # P35G-0-20-C
Tungsten needles		
Microscopes and Imaging machines		
Nikon SMZ800N	Nikon	
Leica TCS SP8 digital light sheet (DLS)	Leica	
Imager M2	Zeiss	
LSM 880 confocal microscope, with Airyscan	Zeiss	
Quanta FEG 250 SEM (serial block face scanning electron microscope)	FEI	
Experimental Models: Organisms/Strains		
<i>Et(-26.5Hsa.WT1-gata2:eGFP)^{cn1} (epi:eGFP)</i>	(Peralta et al., 2013)	ZDB-ETCONSTRCT-170823-1

REAGENT/RESOURCE	SOURCE	IDENTIFIER
<i>Tg(myl7:mRFP)^{ko08Tg}</i>	(Rohr et al., 2008)	ZDB-TGCONSTRCT-080917-1
<i>Tg(fli1a:Gal4)^{ubs3Tg}</i>	(Herwig et al., 2011)	ZDB-ALT-120113-6
<i>Tg(myl7:Gal4)^{cbg2Tg}</i>	(Mickoleit et al., 2014)	ZDB-TGCONSTRCT-150108-1
<i>Tg(-3.5ubi:loxP-eGFP-loxP-mCherry)^{cz1701}</i>	(Mosimann et al., 2011)	ZDB-TGCONSTRCT-110124-1
<i>Tg(eGFP:5xUAS:RFP; gcryst:cerulean)^{cn15}</i>	(Sanz-Morejon et al., 2019)	ZDB-TGCONSTRCT-190724-4
<i>Tg(wt1a:CreERT2);^{cn10Tg}</i>	(Sánchez-Iranzo et al., 2018)	ZDB-TGCONSTRCT-170711-9
<i>Tg(-3.5ubi:loxP-EGFP-loxP-mCherry)^{cz1701Tg}</i>	(Mosimann et al., 2011)	ZDB-ALT-110124-1
<i>Tg(bGI-eGFP:5xUAS:wt1b - bGI; cryaa:eCFP)^{brn4}</i>	This manuscript	ZDB-ALT-200327-14
<i>Tg(bactin2:loxP-DsRed2-loxP-eGFP-T2A-wt1a)^{ji21}</i>	This manuscript	N/A
<i>Tg(bGI-eGFP:5xUAS:tcf21 - bGI; cryaa:eCFP)^{brn5}</i>	This manuscript	N/A